The Interaction between Low-Level Jets and Cold Pools and Their Impacts on Convection

DONG FU,[a,b,c] YU DU,[a,b,c] AND HONGPEI YANG[a,b,c]

[a] *School of Atmospheric Sciences, Sun Yat-sen University and Southern Marine Science and Engineering Guangdong Laboratory (Zhuhai), Zhuhai, China*
[b] *Guangdong Province Key Laboratory for Climate Change and Natural Disaster Studies, Sun Yat-sen University, Zhuhai, China*
[c] *Key Laboratory of Tropical Atmosphere-Ocean System, Ministry of Education, Sun Yat-sen University, Zhuhai, China*

(Manuscript received 23 January 2025, in final form 5 March 2026, accepted 27 March 2026)

ABSTRACT: Previous studies have investigated the optimal configuration of squall lines under unidirectional shear and cold pool interactions [Rotunno–Klemp–Weisman (RKW) theory], but the role of low-level jets (LLJs) with more complex shear remains unclear. This study utilizes idealized numerical simulations to examine the impacts of LLJs on cold pools and their role in convection, focusing on the sensitivity to LLJ height and strength. Simulations reveal that under the influence of an LLJ, a cold pool typically evolves into a two-step structure with two distinct heads and decays more rapidly than other scenarios. Two prominent regions of upward motion emerge near these heads, with one associated with the aloft head, facilitating elevated convection initiation. Differences in horizontal vorticity above and below the jet core lead to contrasting parcel lifting and trajectory clustering: two distinct clusters during the initiation phase and multiple scattered clusters during the mature phase, resulting in a less-organized convective system. A weaker or lower LLJ promotes earlier convection initiation due to enhanced preinitiation vertical motion driven by LLJ–cold pool interactions. In the mature stage, the strongest convection develops under LLJ configurations with optimal height and strength, where the horizontal vorticity pairing above the jet core aligns with RKW theory.

SIGNIFICANCE STATEMENT: While the interaction between unidirectional vertical wind shear and surface cold pools is well understood in maintaining convection, the dynamics between low-level jets (LLJs), which are characterized by more complex wind profiles, and cold pools remain unclear. This study investigates the LLJ–cold pool interaction and its impact on convection. The presence of LLJs modifies cold pool structure and updraft dynamics, influencing both the initiation timing and the intensity of convection. This research enhances our understanding of the intricate relationships between cold pools and environmental wind shear, ultimately improving predictions of mesoscale convection.

KEYWORDS: Convection; Density currents; Dynamics; Shear structure/flows; Vertical motion; Wind shear

1. Introduction

Cold pools are near-surface areas formed by the descent of cold air due to precipitation evaporation and cooling (Goff 1976; Zipser 1977). As the cold and dense outflow spreads, the interface between the outflow and the ambient warm air is referred to as the leading edge of the cold pool or a density current (Charba 1974). The vertical bulge at the front of the cold air, often accompanied by circulation features such as billows or lobes, is termed the cold pool head, while the main body of the cold pool is relatively flat and shallow.

New convective cells are often triggered when warm, moist environmental air is mechanically lifted at the leading edge of the cold pool (Goff 1976; Purdom 1976; Feng et al. 2015; Simoes-Sousa et al. 2022; Mai et al. 2025). Cold pools also play an important role in the organization of mesoscale convective systems (Torri et al. 2015). In tropical regions, cold pools help cumulus congestus reach the midtroposphere, thereby influencing regional weather and climate (Chandra et al. 2018). When cold pools intersect, as opposed to isolated ones, they can promote deeper convection by generating more closely spaced and larger clouds (Feng et al. 2015). However, a persistent cold pool may suppress surface-based convection initiation (CI) due to low-level stabilization (Trapp and Woznicki 2017). Therefore, cold pools generated from parent convective systems significantly influence the initiation, intensity, and life cycle of the secondary convection (Zipser 1977; Marion and Trapp 2019; Borque et al. 2020; Yang and Du 2026).

Previous studies have demonstrated that cold pool dynamics are highly sensitive to ambient winds (e.g., Parker 1996; Thorpe et al. 1982). Parker (1996), using a three-dimensional numerical simulation, found that the cold pool shape is more significantly affected by the ambient wind strength than by the magnitude of vertical wind shear. Chen (1995) revealed that the depth of cold pools depends on both the magnitude and direction of wind shear, with a positive wind shear, where the shear vector aligns with the movement direction of the cold pool, producing a deeper cold pool. Sufficiently strong positive shear can cause the cold pool to develop a more spread-out structure with two different heads. Additionally, enhanced positive shear can increase the propagation speed of cold pools (Xu 1992). At the upper interface of cold pools, turbulent mixing driven by cross-interface shear often generates Kelvin–Helmholtz (KH) billows, leading

Corresponding author: Yu Du, duyu7@mail.sysu.edu.cn

DOI: 10.1175/JAS-D-25-0013.1

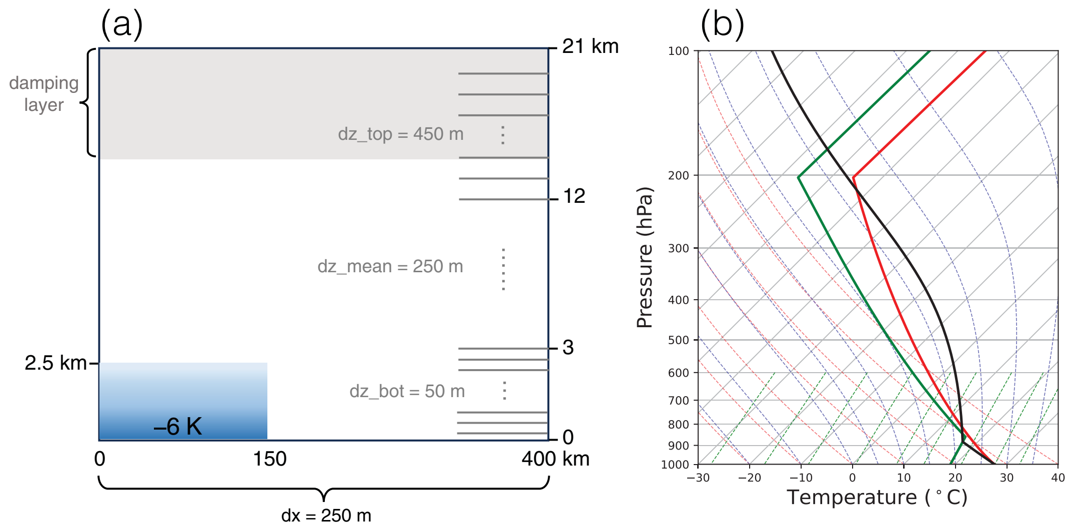

FIG. 1. (a) CM1 initial conditions. The dark blue shade depicts the initial cold pool, which is 150 km wide and 2.5 km deep. The x axis is horizontal distance (km), and the z axis is vertical distance (km). (b) Skew T–log$p$ diagram of the sounding for the simulations. The black line denotes the parcel path from the surface, while the red and green lines represent the temperature and dewpoint temperature, respectively.

to updraft–downdraft couplets (e.g., Droegemeier and Wilhelmson 1987; Xue 2002; Grant and van den Heever 2016).

The Rotunno–Klemp–Weisman (RKW) theory, named after Rotunno et al. (1988), provides a conceptual framework for understanding the balance of horizontal vorticity between cold pool dynamics and environmental wind shear in organizing and maintaining mesoscale convective systems. The theory emphasizes the importance of the relative balance between the cold pool's negative horizontal vorticity and the positive horizontal vorticity from the vertical wind shear for optimal lifting and convection (Rotunno et al. 1988; Weisman and Rotunno 2004). This optimal state can be quantitatively assessed using the ratio of cold pool intensity (C) to the net vertical change in horizontal velocity (ΔU). Specifically, when $C/\Delta U \approx 1$, environmental conditions are most conducive to the development of convection.

Numerical modeling studies have shown that the overall development and structure of convective systems are closely linked to this ratio (e.g., Weisman 1992, 1993; Bryan et al. 2006). While some studies reported that many strong, long-lived squall lines occur even when $C/\Delta U > 1$ (e.g., Evans and Doswell 2001; Coniglio et al. 2004; Stensrud et al. 2005), Bryan et al. (2006) showed that across four numerical models, the system vertical structure strongly depends on the interplay between the cold pool and environmental shear. They found that when $C/\Delta U \approx 1$, convective systems tend to be more upright and symmetric, featuring stronger updrafts, higher rainfall rates, and more intense surface winds. Bryan and Rotunno (2014) further theoretically demonstrated that the lifting of environmental air is influenced by the depth and strength of wind shear. Recent studies have applied this theory to both real and idealized cases (Li et al. 2021; Alfaro and Lezana 2022; Zhao et al. 2024). For instance, Alfaro and Lezana (2022) revealed that downwind slanted updrafts can develop when $C/\Delta U > 1$, while $C/\Delta U < 1$ can favor upwind updrafts, highlighting the strong sensitivity of updraft orientation to vertical shear strength—an idea also supported by Bryan and Rotunno (2014). In a simulation of a squall line event in South China, Zhao et al. (2024) found that as the squall line moved from the mountains to the plains, the cold pool weakened while vertical wind shear increased, resulting $C/\Delta U = 0.9$. This change in conditions facilitated the low-level convergence and the development of updrafts, thereby contributing to the maintenance of the squall line.

However, most previous studies have focused on simple unidirectional shear, where the shear vector maintains a consistent direction with height, leaving the effects of more complex wind profiles, such as those associated with low-level jets (LLJs), less explored. To address this gap, this study examines how LLJs influence cold pool dynamics and the initiation and development of convection, comparing their interaction mechanisms to those observed under unidirectional shear conditions. An LLJ is characterized by a wind speed maximum in the lower troposphere, with a nose-like wind profile and sharp wind speed decreases both above and below the jet core (Shapiro and Fedorovich 2010; Du and Rotunno 2014; Luiz and Fiedler 2024). This unique jet structure generates vertical wind shear with opposing directions and horizontal vorticities below and above the jet core. The strong low-level wind speeds of LLJs facilitate the transport of moist air and strengthen low-level convergence, thereby promoting lifting mechanisms conducive to convective development (e.g., Trier et al. 2006; Vera et al. 2006; Du et al. 2020a,b; Luo and Du 2023). In addition, LLJ-induced shear plays a critical role in turbulent mixing and significantly influences the structure of the boundary layer (Hu et al. 2013; Banta et al. 2003; Fu et al. 2025).

In contrast to the well-studied effects of unidirectional shear, the role of LLJs in interacting with cold pools is more complicated. In a review article, Fritsch and Forbes (2001) suggested that when LLJs overrun frontal zones, the shear below the jet core that shares the same vorticity sign as the cold pool will promote a slantwise convective ascent along the cold pool

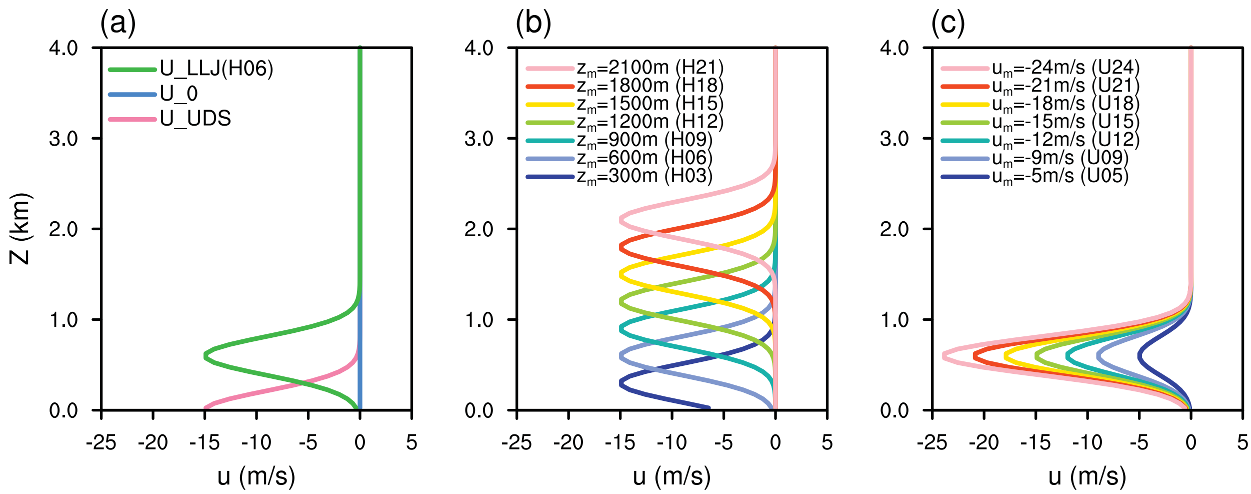

FIG. 2. Vertical wind profiles (u component) used in simulations for (a) different wind profile types, (b) LLJs at varying heights, and (c) LLJs at varying strengths.

boundary, thereby accelerating the expansion of the stratiform region. Parker (2008) and Schumacher (2009) found that LLJs facilitate the transition of convective systems from surface-based to elevated states, with the lifting mechanism evolving from a cold pool to a bore within a stable boundary layer. French and Parker (2010) further investigated the effects of LLJ-associated wind shear and changes in storm-relative inflow on convective systems through numerical experiments. They found that below-jet shear is crucial for surface-based systems, while above-jet shear becomes more important as the system transitions to an elevated state. More recently, Hitchcock and Schumacher (2020) conducted idealized simulations to examine how LLJ-induced vertical wind shear interacts with an intrusion, where the upper and lower layers exhibit relative negative and positive buoyancy, respectively, leading to varying response to lifting on the upshear or downshear side. Despite these valuable contributions, the direct impact of variations in the vertical structure of LLJs on cold pool dynamics and lifting

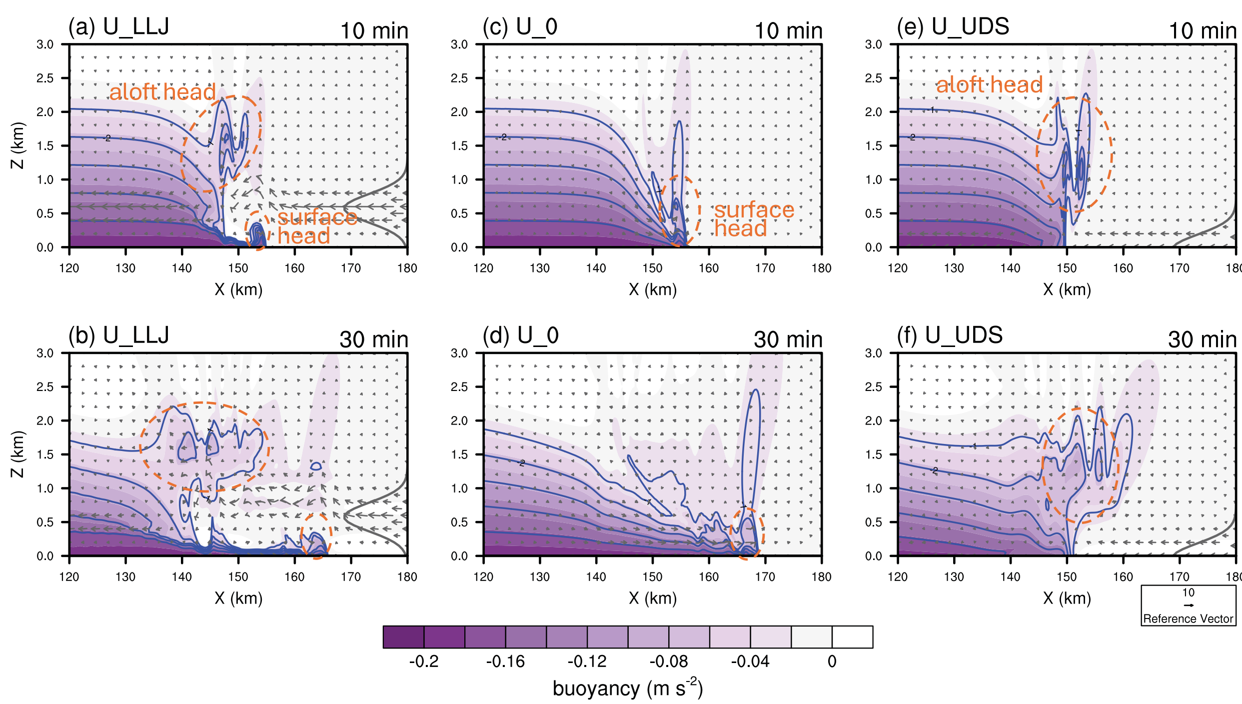

FIG. 3. Line-averaged vertical cross sections of buoyancy (m s^{-2}; shaded), wind vectors (m s^{-1}; u and w), and potential temperature perturbation (K; blue contours every -1 K starting from -1 K) for (a),(b) U_LLJ, (c),(d) U_0, and (e),(f) U_UDS simulations at (a),(c),(e) $t = 10$ min and (b),(d),(f) 30 min. The gray lines indicate the vertical profiles of horizontal wind speed for each scenario.

mechanisms, particularly in contrast to unidirectional shear, remains insufficiently explored.

The interactions between the LLJs and cold pools are influenced by several factors, including the orientation, strength, and height of the LLJ, as well as the depth, width, and intensity of the cold pool. Given the complexity of these interactions, this study focuses specifically on LLJ height and strength, systematically investigating how their variations influence cold pool structure, lifting processes, and the evolution of convective systems. Section 2 introduces the model configuration used in the idealized simulations. Sections 3 and 4 compare three scenarios, including no wind, unidirectional shear, and LLJ, to explore how the LLJ affects cold pool structure, lifting, and convection. Section 5 examines the sensitivity of their interactions to variations in LLJ height and strength. Finally, a summary and discussion of findings are provided in section 6.

2. Model configuration

The idealized Cloud Model 1 (CM1, version 20.3; Bryan and Fritsch 2002) was used for the numerical simulations. The model was configured in a three-dimensional domain, with an initial thermodynamic sounding (Weisman and Klemp 1982) as shown in Fig. 1. The domain was 400 km in the x direction and 200 km in the y direction with a horizontal grid spacing of 250 m and 21 km in the z direction. The vertical grid spacing was set to 50 m in the lowest 3 km and stretched to 450 m above 12 km. Open-radiative lateral boundary conditions were applied in the east–west (cross-line) direction, while periodic boundary conditions were imposed along the north–south (along-line) direction. The upper and lower boundary conditions were set to free-slip, and a Rayleigh damping layer was applied above 15 km, with an inverse e-folding time scale of 1/300 s^{-1}. Subgrid turbulence was parameterized using a prognostic scheme for turbulent kinetic energy (TKE). The time step for the simulations was 2 s, and the implicit Klemp–Wilhelmson time splitting method was employed to solve for pressure vertically (Klemp and Wilhelmson 1978).

The cold pool was initialized using the "dam break style" method, in which a block of cold air was situated at the western edge of the domain (Weisman et al. 1997). This cold block extended uniformly across the entire y direction, with a depth of 2.5 km, a width of 150 km in the x direction, and a maximum potential temperature deficit of -6 K at the surface, decreasing linearly to zero at a height of 2.5 km. A small random potential temperature perturbation (0.1 K) was added to the cold block to promote the development of three-dimensional structures (Weisman and Rotunno 2004). The uniform extension in the y direction minimized artificial lateral gradients and reduced unintended convective initiation near the northern and southern edges of the cold pool, allowing the focus to remain on its interaction with the LLJ along the eastern edge. The initial thermodynamic conditions, including temperature and moisture profiles, were based on those from Weisman and Klemp (1982), representing moderate convective available potential energy (CAPE). For the moist simulations in sections 4 and 5, the initial surface mixing ratio (q_v) was set to 14.0 g kg^{-1}. In the dry simulations discussed in section 3, the configuration remained unchanged,

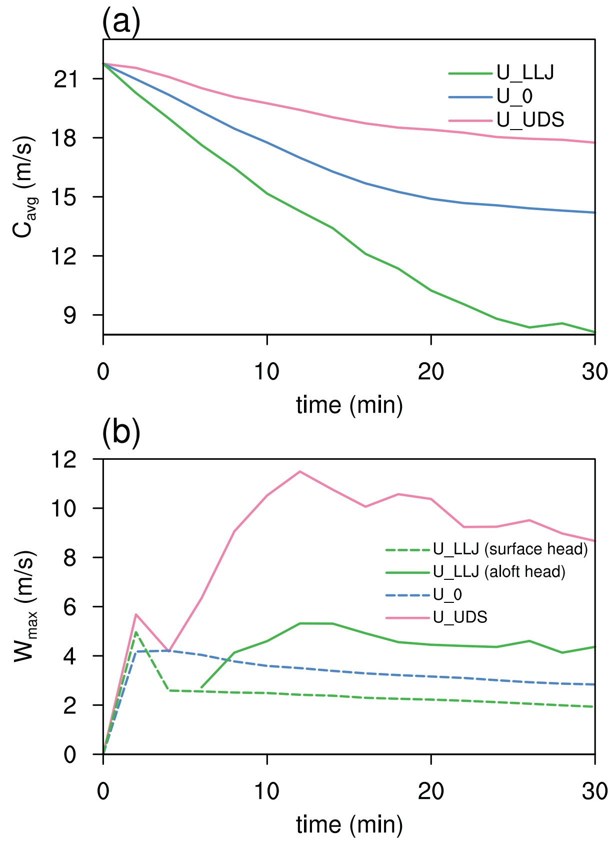

FIG. 4. Time series of (a) average cold pool intensity (m s^{-1}), computed over the 20-km region behind the leading edge of the cold pool, and (b) maximum vertical velocity (m s^{-1}) for the U_0 (blue line), U_LLJ (green line; dashed and solid lines for vertical motions near the regions of the surface head and aloft head, respectively), and U_UDS (pink line) simulations.

except that moist processes were disabled. In addition, all simulations were integrated for 4 h, during which the cold pool and associated convection remained within the computational domain.

To investigate the interaction between the LLJ and the cold pool, a control simulation (U_LLJ) was conducted using the LLJ vertical wind profile (green line in Fig. 2a). The profile follows a Gaussian function, defined as

$$u(z) = u_m \exp\left[-\frac{(z - z_m)^2}{\sigma^2}\right],$$

where u_m is the maximum wind speed at the height of the jet core (z_m) and the parameter σ represents the standard deviation that determines the shape of the wind profile, which was set to 300 m for all LLJ simulations. The u-component wind profile had a maximum speed of -15 m s^{-1} at $z = z_m = 600$ m, consistent with the wind structure of observed southerly LLJs in the Southern Great Plains (Whiteman et al. 1997). In our configuration, the LLJ is oriented perpendicular to the cold pool, such that vertical wind shear is primarily normal to the convective

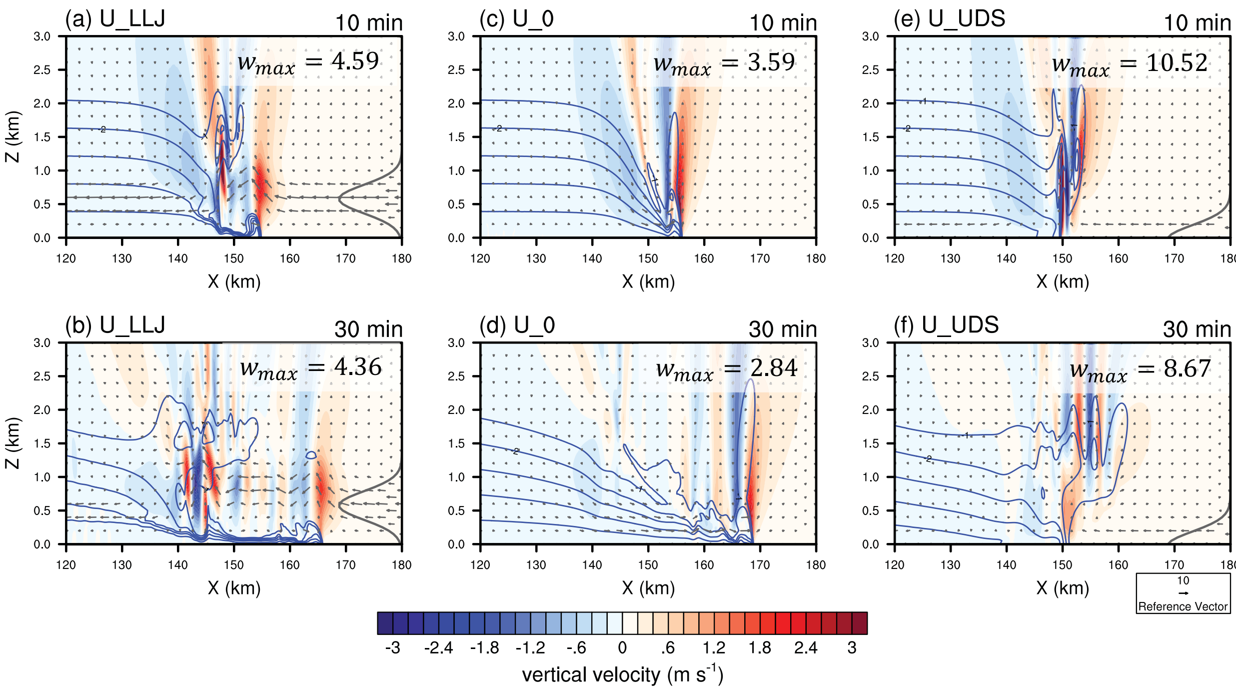

FIG. 5. As in Fig. 3, but for vertical velocity (m s^{-1}; shaded). The maximum vertical velocity (m s^{-1}) near the cold pool head is given in each panel.

system with a minimal along-line component. Prior work indicates that such a perpendicular arrangement between the LLJ and cold pool front can lead to the strongest interaction (e.g., French and Parker 2010). Nonetheless, cases with LLJs parallel to the convective line are also observed, and the resulting LLJ–cold pool interaction may differ, warranting future study.

For comparison, two additional sensitivity experiments were performed: one with no u-component background winds (U_0, blue line in Fig. 2a) and another with a unidirectional shear profile in the u component (U_UDS, pink line in Fig. 2a), where the shear vector points in a single direction, similar to that applied in RKW theory (Rotunno et al. 1988). The unidirectional shear profile is characterized by a maximum speed of -15 m s^{-1} at the surface directed toward the cold pool. Unlike the 2.5-km-deep shear layer commonly used in RKW studies, the unidirectional shear here was confined to the lowest 1 km to facilitate a more direct comparison with the U_LLJ case, as both profiles share an identical shear structure above the height of maximum wind speed.

To evaluate the upward velocity and parcel motion trajectories as a response to cold pool–LLJ interaction, a total of 17 500 Lagrangian parcels were initialized within the simulation domain on a 70 (x direction) × 10 (y direction) × 25 (z direction) grid. Horizontally, the initial parcels were spaced at 1-km intervals in both the x and y directions, extending northward from y = 20 km and eastward from the leading edge of the cold pool at x = 150 km. Vertically, the parcels were positioned every 100 m, extending from the surface to a height of 2.5 km. As the simulation progressed, the movement of parcels was influenced by both the cold pool and the surrounding winds. The position and velocity of each parcel were recorded at 1-min intervals, enabling a detailed analysis of the interaction between the LLJ and the cold pool.

3. Interaction between low-level jet and cold pool

a. Cold pool evolution

The evolution of cold pools under varying vertical wind profiles, including LLJ, no wind, and unidirectional shear, is shown in Fig. 3. In all three cases, cold pools, marked by regions of negative buoyancy, gradually propagate eastward along the surface, with their leading edge extending beyond the initial position at x = 150 km. As the cold air within the cold pools mixes with the surrounding warmer air, the intensity of the cold pools weakens over time (Fig. 4a), consistent with Weisman et al. (1997). The rate of cold pool weakening, however, varies significantly depending on the background wind profile. The cold pool intensity (C), representing the theoretical speed of a two-dimensional cold pool, is given by Weisman (1992):

$$C = \sqrt{-2\int_0^{z_c} B\, dz},$$

where B is the line-averaged buoyancy in the y direction, computed over the 20-km region in the x direction extending behind the cold pool leading edge, and z_c is the top boundary of the cold pool, defined as the height where buoyancy becomes zero.

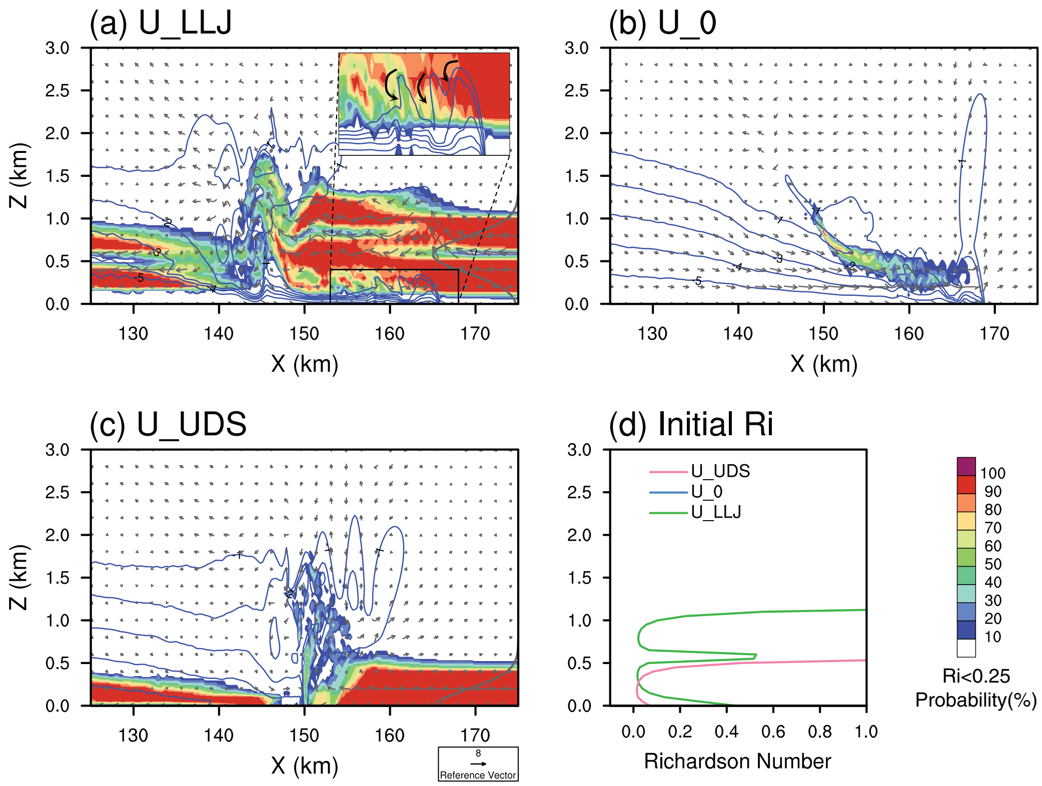

FIG. 6. Probability (%; shaded) of small Richardson number ($0 < \mathrm{Ri} < 0.25$) during the 10–30-min period, wind vectors (m s^{-1}), and potential temperature perturbation (K; blue contours every -1 K starting from -1 K) at $t = 30$ min for (a) U_LLJ, (b) U_0, and (c) U_UDS simulations. The gray lines indicate the vertical profiles of horizontal wind speed for each scenario. A zoomed-in view of the cold pool surface head is also embedded in (a), with arrows indicating the KH billows. (d) The background Ri vertical profiles for different wind profile types. Note that the U_0 case is hardly discernible due to extremely large Ri values.

In the U_UDS case, the average cold pool intensity decreases to 18 m s^{-1} within 30 min, while in the U_LLJ case, it drops below 9 m s^{-1}, with a reduction of more than 12 m s^{-1} from the initial value (Fig. 4a). Notably, the presence of the LLJ leads to a more rapid weakening of the cold pool compared to the unidirectional shear and no-wind scenarios. This enhanced weakening in the LLJ scenario may result from two processes: 1) increased turbulence near the jet core, which accelerates mixing and dilution of the cold pool, as discussed further in the following section, and 2) stronger cold pool–LLJ shear interactions, which promote more horizontal spreading and reduce the vertical lifting efficiency (Hitchcock and Schumacher 2020). In contrast, the minimal ambient shear in the U_0 simulation results in slower cold pool reduction due to the weak interaction with the background flow (Fig. 4a).

Interestingly, in the U_LLJ simulation, the low-level leading edge of the cold pool moves further eastward due to the weak opposing background wind near the surface. However, the main body of the cold pool is largely obstructed at the original position of its leading edge by the strong winds near the jet core (Figs. 3a,b). This interaction causes the cold pool to evolve into a two-step structure with two distinct heads, accompanied by vertical circulation features (indicated by orange circles): one near the surface and the other aloft, around 2-km altitude. Specifically, the aloft head remains nearly stationary, while the surface head continues to advance eastward as the cold pool spreads. This two-step structure of the density current resembles the behavior of a sea-breeze front, which similarly evolves into a double-head structure after reaching its mature phase (Chen et al. 2019). Additionally, small-scale buoyancy disturbances are observed near both heads, likely caused by turbulent mixing generated through the interaction between jet-induced shear and the cold pool. A more detailed discussion of these processes is provided in section 3b.

In contrast, the cold pools in the U_0 (no wind) and U_UDS (unidirectional shear) simulations do not develop a two-step structure; instead, they exhibit a single head. In the U_0 scenario, similar to U_LLJ, the cold pool spreads rapidly in the absence of near-surface wind, with its surface head characterized by weakened negative buoyancy (Figs. 3c,d). Conversely, in the U_UDS scenario, the strong opposing winds near the surface act as a barrier, preventing significant diffusion of the cold pool at lower levels. As a result, the cold air tends to accumulate and spread aloft, leading to the formation of a more pronounced aloft head, and the cold pool experiences the least weakening (Figs. 3e,f and 4a).

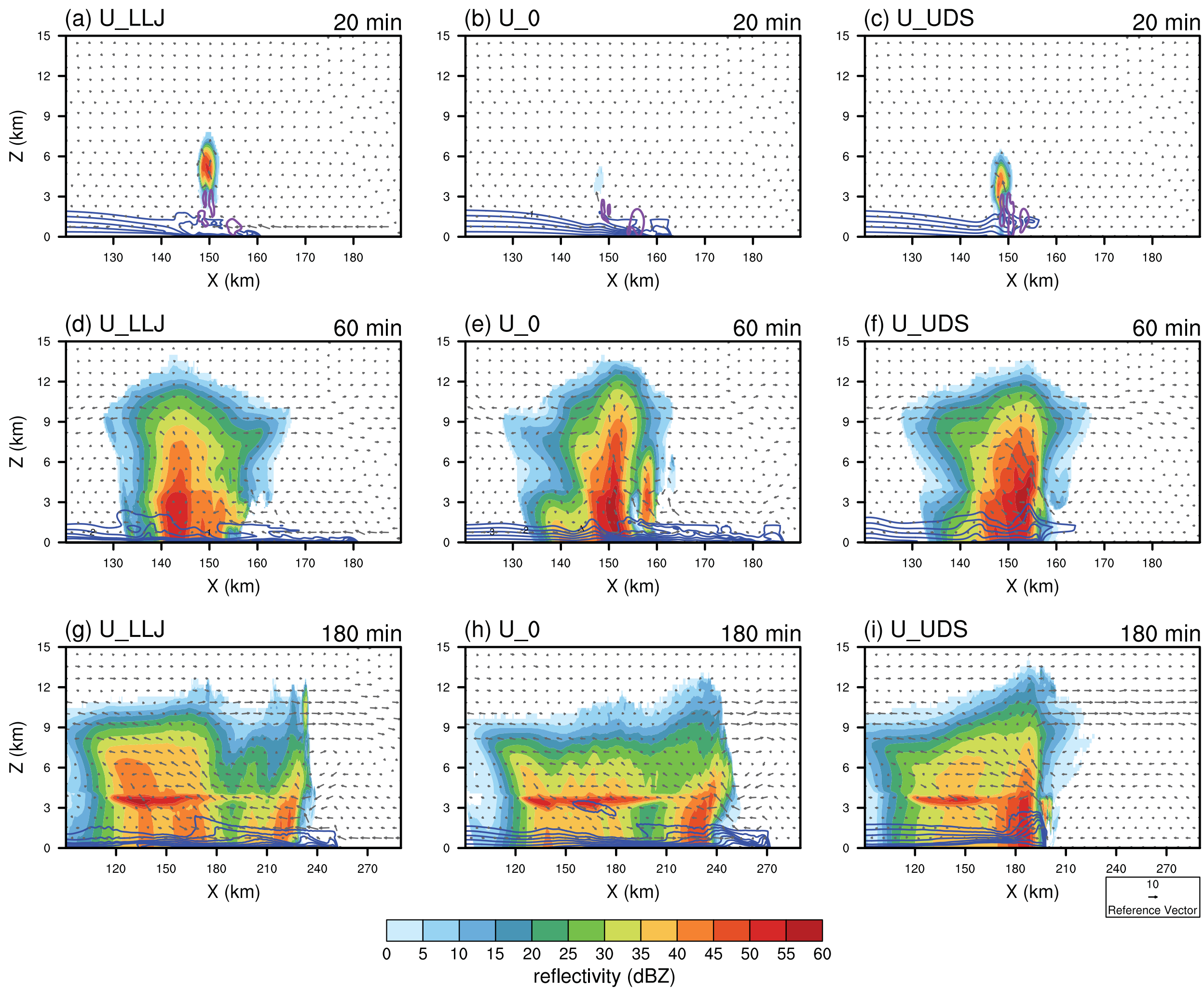

FIG. 7. Line-averaged vertical cross sections of radar reflectivity (dBZ; shaded), wind vectors (m s^{-1}), potential temperature perturbation (K; blue contours every -1 K starting from -1 K), and updraft speed 2 min prior to convection initiation (purple contour at 1 m s^{-1}) for (a),(d),(g) U_LLJ, (b),(e),(h) U_0, and (c),(f),(i) U_UDS simulations at (a)–(c) t = 20 min, (d)–(f) 60 min, and (g)–(i) 180 min.

A noteworthy aspect of the U_UDS simulation is that the imposed unidirectional shear is only about 1 km deep, while the cold pool depth is approximately 2 km. This yields the ratio of shear layer depth (h) to the cold pool depth (H) of about 1/2, which is substantially lower than the optimal ratio ($h/H \approx 3/4$) identified by Bryan and Rotunno (2014) for maximizing updraft strength. Under such suboptimal conditions, Bryan and Rotunno (2014) showed that the updraft tends to tilt away from the cold pool with height (see their Fig. 18a), and the ascending flow is finally lifted above the initial shear layer. A similar updraft tilt structure is evident in our Figs. 3e and 3f.

b. Cold pool lifting and shear instability

The vertical motion associated with the cold pools is shown in Fig. 5. As discussed earlier, the cold pool affected by the LLJ develops two distinct heads over time. Consequently, two separate regions of significant vertical motion develop: one associated with the surface head and the other with the aloft head (Figs. 5a,b). The vertical motion near the aloft head becomes notably enhanced approximately 6 min after it separates from the surface head, reaching a maximum vertical velocity of more than 5.32 m s^{-1} at t = 12 min (Fig. 4b). As the surface head continues to progress eastward, the distance between these two regions of vertical motion increases. By t = 30 min, the lifting produced by the aloft head remains more pronounced than the vertical motion by the surface head, with maximum vertical velocities of 4.36 and 1.93 m s^{-1}, respectively (Figs. 4b and 5b).

In the U_0 case, convergence between the relatively shallow cold pool head and the surrounding warm air is the weakest, diminishing as the cold pool weakens over time (Figs. 4b and 5c,d). In contrast, the U_UDS case produces the most intense

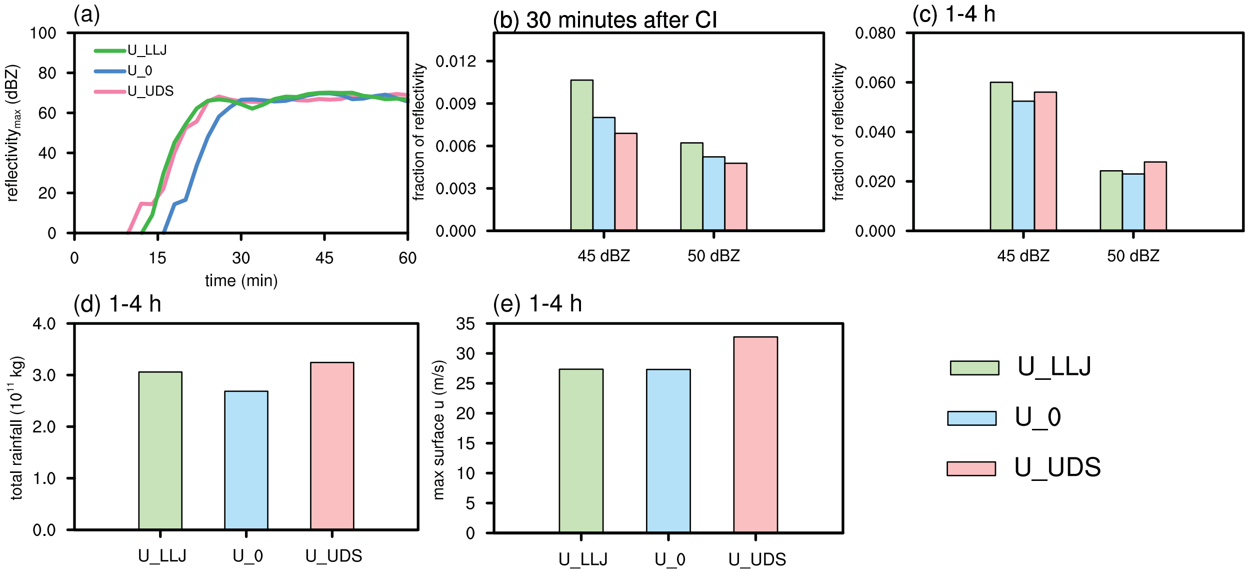

FIG. 8. (a) Time series of maximum radar reflectivity (dBZ), (b) fraction of radar reflectivity exceeding 45 and 50 dBZ during the 30-min period after convection initiation, and system intensity metrics during the mature phase (1–4 h): (c) fraction of radar reflectivity exceeding 45 and 50 dBZ, (d) total accumulated rainfall (10^{11} kg), and (e) maximum outflow (m s^{-1}; defined as surface wind relative to the LLJ background flow at the lowest model level) for U_LLJ (green), U_0 (blue), and U_UDS (pink) simulations.

vertical motion, exceeding 10.5 m s^{-1} at t = 10 min, owing to the enhanced interaction between the thicker cold pool head and the opposing background winds (Figs. 4b and 5e,f). To assess the sensitivity of lifting intensity to shear depth, an additional simulation was performed using a deeper RKW-type shear profile, with wind speed decreasing linearly from -15 m s^{-1} at the surface to 0 m s^{-1} at 2.5-km altitude. Compared to the shallower shear layer in U_UDS, this additional simulation produces stronger and more upright lifting along the cold pool's leading edge (not shown), consistent with the optimal h/H ratio proposed by Bryan and Rotunno (2014).

Shear instability, characterized by a small Richardson number, is primarily driven by the strong vertical wind shear both above and beneath the jet core, as well as the intrusion of ambient warm air near the cold pool head, as shown in Fig. 6. The unique structure of the LLJ, with its opposite vertical wind shear, enhances its interaction with cold pools (Figs. 3b and 5b). This interaction triggers intense turbulence, particularly in regions of strong shear, which promotes mixing with the warmer surrounding air and accelerates the weakening of the cold pool (Figs. 4a and 6a). At low levels (~0.2 km, below the jet core), KH billows are evident near the cold pool edge, characterized by partially rolled-up structures indicative of shear-driven instability (black arrows in Fig. 6a). Above the jet core, shear instability further promotes small-scale disturbances (Sha et al. 1991; Plant and Keith 2007), leading to upward and downward motions (i.e., wave-like vertical motions) near the aloft head of U_LLJ simulations (Figs. 5b and 6a). Such small-scale vertical perturbations are also observed near the head in U_UDS (Figs. 5f and 6c). In contrast, these features are largely absent in the U_0 case due to the absence of ambient vertical wind shear (Fig. 6b).

4. Convection through LLJ and cold pool interaction

In this section, we discuss how convection is initiated and evolves through the interaction between the LLJ and the cold pool. We conducted three similar simulations as in section 3 (U_LLJ, U_0, and U_UDS), but with moist processes enabled. In these moist simulations, convection consistently initiates near the original leading edge of the cold pools ($x \sim 150$ km), coinciding with the first appearance of prominent uplift in this region prior to 20 min in all cases (Figs. 7a–c). Despite the presence of weak vertical motion near the surface head in either LLJ or no-wind cases (Fig. 5), these ascents are insufficient to lift air parcels to the level of free convection (LFC) or to overcome the convective inhibition (CIN) (not shown), thus failing to initiate convection.

As convection intensifies, the echoes expand both horizontally and vertically by 60 min, marking the growth of the convective system (Figs. 7d–f). Notably, in the U_LLJ simulation, the convective system becomes less organized, leading to larger horizontal coverage of high reflectivity at t = 60 min. In contrast, the U_UDS case exhibits organized convective structures behind the leading edge of the cold pool. By 180 min, as the cold pools spread eastward, convection in both the U_LLJ and U_0 also extends to approximately 230 km, accompanied by an expansion of the stratiform precipitation area (Figs. 7g,h). In U_UDS, however, stronger surface winds slow the cold pool propagation to about 200 km, thereby restricting total convective coverage but producing a more intense convective precipitation area (Fig. 7i).

When comparing the three cases, convection initiates earliest (>0 dBZ after 12 min) in the U_UDS simulation (pink line in Fig. 8a), which is consistent with the strongest vertical motion observed in the dry simulation (pink line in Fig. 4b).

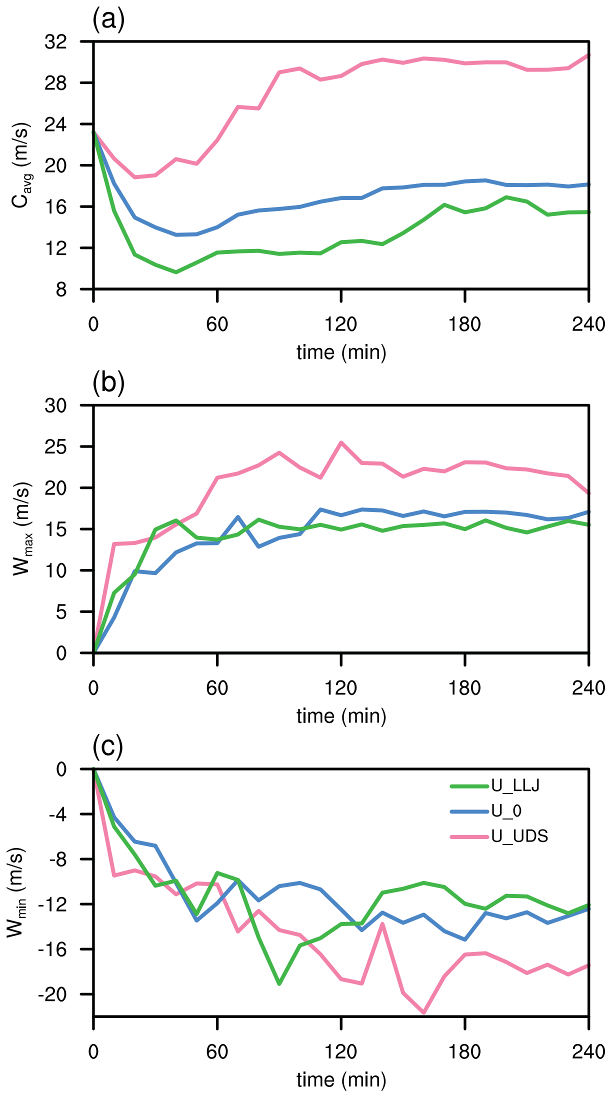

FIG. 9. Time series of (a) average cold pool intensity (m s^{-1}), calculated between the leading edge of the cold pool and 20 km behind it, (b) the maximum vertical velocity (m s^{-1}), and (c) maximum downdraft velocity (m s^{-1}) for the U_LLJ (green), U_0 (blue), and U_UDS (pink) simulations.

In contrast, convection initiates later around 14 min in U_LLJ (green line in Fig. 8a), likely due to the weaker vertical motion above the jet core and negligible upward motion below it prior to initiation (Fig. 4b). The U_0 case, where the dry vertical velocity is the smallest, shows the most delayed CI (blue lines in Figs. 4b and 8a).

To examine the influence of vertical wind profiles on the early development of convective systems (i.e., convection initiation phase), we quantified the fraction of radar reflectivity exceeding 45 or 50 dB*Z* during the 30 min following convection initiation (Fig. 8b). Additionally, the high reflectivity fraction, accumulated rainfall, and maximum surface wind during the 1–4-h window were used to characterize the system intensity during the mature phase (Bryan et al. 2006; Figs. 8c–e).

During the convection initiation phase, the U_LLJ case exhibits a higher fraction of intense reflectivity compared to U_UDS—approximately 40% more area with reflectivity exceeding 45 dB*Z*—suggesting that the presence of an LLJ may promote stronger initial convective development (Fig. 8b). A similar enhancement is observed in U_0, although its high-reflectivity fraction is smaller than that in U_LLJ but larger than that in U_UDS. This finding will be further explored later. During the mature phase (1–4 h), the fraction of high reflectivity remains greater in the U_LLJ case, likely due to the broader convective coverage (Figs. 7g and 8c). However, the U_UDS case generates a more intense convective system, producing the greatest rainfall and strongest surface winds among all cases (Figs. 8d,e). These results align with the dry experiments, where the cold pool–shear interaction in the U_UDS scenario supports the most robust updrafts.

The time series of maximum updrafts and downdrafts effectively illustrate the convective evolution (Figs. 9b,c). In the U_UDS simulation, both updrafts and downdrafts intensify markedly, particularly after 40 min. The intensified downdrafts contribute to a more pronounced average cold pool intensity (Fig. 9a), consistent with the enhanced convective system observed during the mature phase (Figs. 8d,e). In contrast, the U_LLJ and U_0 simulations exhibit comparatively slower enhancement rates, resulting in less intense convective systems during the mature phase.

To better distinguish the convection modes, parcel trajectories associated with the updrafts were examined (Fig. 10). The trajectory patterns suggest that convection in the U_LLJ and U_0 simulations develops in an elevated manner (Figs. 10a,b), whereas convection in the U_UDS case is primarily surface based (Fig. 10c). In the U_LLJ case, parcels associated with the convective updrafts (exceeding 3 m s^{-1}) predominantly originate from heights near the jet core (30 min, Fig. 10a). Specifically, two distinct clusters of parcel trajectories are observed in the U_LLJ case. Cluster A primarily consists of parcels originating from above the jet core (Figs. 10a and 11a), where the positive environmental horizontal vorticity associated with the above-jet shear interacts with the negative horizontal vorticity from the cold pool, reducing the rearward tilting tendency and promoting a more upright ascent once parcels become convective. This enables parcels to reach their LFC more efficiently. In contrast, cluster B (Figs. 10a and 11a) mainly consists of parcels below the jet core, where both the horizontal vorticity associated with the below-jet shear and that from the cold pool have the same sign, reinforcing the rearward tilt toward the cold pool side, delaying vertical ascent and causing parcels to require more time to reach their LFC.

By 60 min into the simulation, multiple air parcel clusters developed due to the negative horizontal vorticity beneath the jet core (Fig. 10d). This behavior likely contributes to the formation of less organized convection and may also support the subsequent development of a broader stratiform region (Figs. 7d,g; Fritsch and Forbes 2001). These findings align with previous studies that vorticity pairing in the same direction inhibits vertical motion and instead facilitates a backward

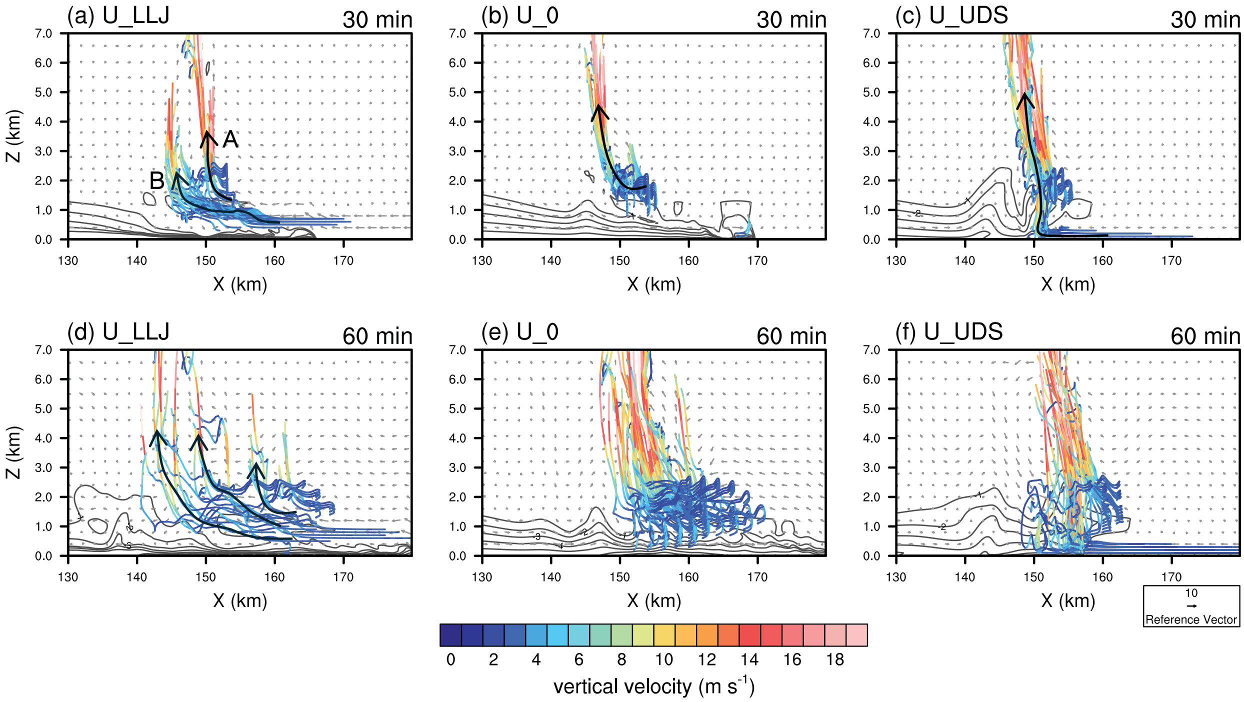

FIG. 10. Parcel trajectories (colored by parcel vertical velocity, m s^{-1}) for parcels within convective updraft during (a)–(c) the first 30 min and (d)–(f) the first 60 min, along with wind vectors (m s^{-1}) and potential temperature perturbation (K; gray contours every -1 K starting from -1 K) at $t = 30$ and 60 min for (a),(d) U_LLJ, (b),(e) U_0, and (c),(f) U_UDS simulations. Parcel trajectories are shown for parcels that experienced upward motion exceeding 3 m s^{-1} aloft.

tilt of the updraft (Rotunno et al. 1988; Weisman et al. 1988; French and Parker 2010; Hitchcock and Schumacher 2020).

In the U_0 case, parcels primarily originate from the region above the surface head, where upward motion is significant (Figs. 5c and 10b). Conversely, in the U_UDS case, parcels originate near the surface, leading to surface-based convection (Figs. 7c and 10c). This behavior is closely related to the surface maximum wind associated with the unidirectional shear. During the mature phase, the U_UDS exhibits the most coherent and organized updraft parcel structures (Fig. 10f), consistent with the convective structures shown earlier.

The vertical distribution of CAPE reveals that elevated CAPE (~2210 J kg^{-1}) exceeds surface CAPE (1860 J kg^{-1}) (red line in Fig. 11b), corresponding to nearly zero elevated CIN (~0 J kg^{-1}) compared to surface CIN (-57 J kg^{-1}) (blue line in Fig. 11b). The higher elevated CAPE and smaller elevated CIN possibly allow more parcels to be lifted above the cold pool, contributing to broader elevated convection and higher radar reflectivity fractions during the initiation phase in the U_LLJ and U_0 cases, where parcels originate from levels with lower CIN (Figs. 10a,b and 11a).

5. Sensitivity to low-level jet height and strength

a. Sensitivity to low-level jet height

To explore how the height of the LLJ affects its interaction with cold pools, we conducted a series of sensitivity experiments where the jet core height (z_m) varied from 300 to 2100 m, while keeping the maximum wind speed ($u_m = -15$ m s^{-1}) and jet shape ($\sigma = 300$ m) constant (Fig. 2b). The interactions between cold pools and LLJs at different heights reveal variations in vertical motions at the leading edge during the early stages (i.e., 2 min before convection initiation, Figs. 12a–c). As the LLJ height rises, both the lifted heights of the maximum updraft and the surface head increase. For instance, in the H06 case, the surface-head height is 0.4 km, and the maximum vertical velocity associated with the surface head is located at nearly 0.7 km, while in the H12 case, these values increase to 0.9 and 1.4 km, respectively.

The time series of the average vertical velocity near the location of convection initiation illustrates the complex evolution of updrafts (Fig. 13a). In lower-altitude LLJ cases (e.g., H03, H06, and H09), the average vertical motion is notably stronger compared to those with higher-altitude cases (e.g., H15, H18, and H21). By $t = 10$ min, the average vertical velocities are still positive in the lower-altitude cases, while they remain weak or even negative in the higher-altitude cases. Meanwhile, the maximum parcel vertical displacements are larger in the lower-altitude LLJ cases (Fig. 13c). This suggests that more effective low-level lifting (i.e., vertical parcel displacements) occurs in a lower-altitude LLJ environment due to stronger convergence by jet–cold pool interaction. Conversely, when the LLJ height is positioned too high relative to the cold pool, their interaction is diminished, leading to weaker ascents.

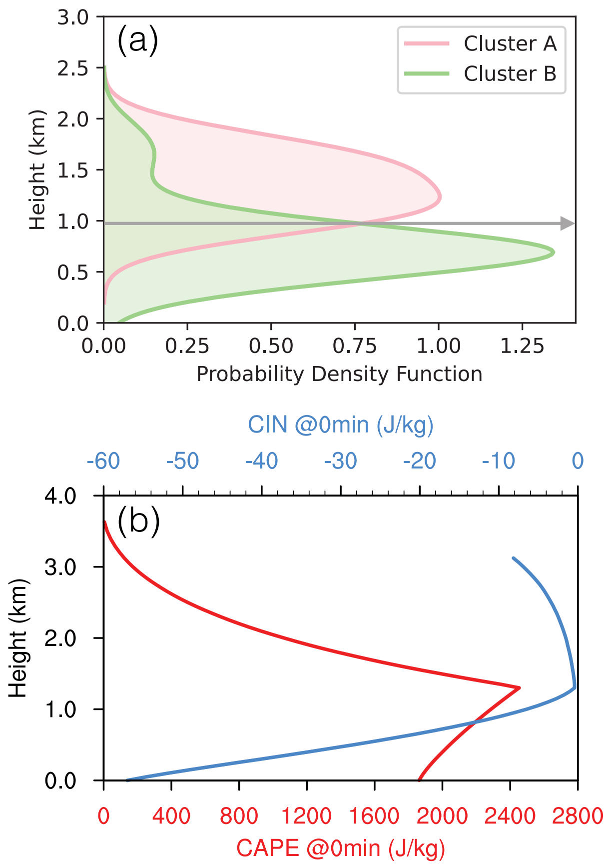

FIG. 11. (a) PDFs of the original height of parcels in the convective updraft for cluster A (pink line) and cluster B (green line) in the U_LLJ simulation. The gray line represents the height of maximum wind speed (jet core) within the cold pool. (b) Vertical distribution of CAPE (J kg^{-1}) and CIN (J kg^{-1}) at t = 0 min for all simulations.

As a result, convection initiates earlier (before t = 12 min) and at roughly the same location (not shown) in the lower-altitude LLJ cases (H03, H06, and H09), with only minimal time differences among them (Fig. 13e). In contrast, convection is delayed in the higher-altitude LLJ cases (e.g., H15, H18, and H21), with initiation not occurring until after around t = 32 min.

During the convection initiation period, a larger fraction of intense reflectivity is observed in simulations with higher LLJ (e.g., H15 and H18 in Fig. 14a) due to larger convective coverage rather than inherently stronger convective intensity. The larger convective systems in H15 and H18 possibly result from prolonged and enhanced accumulation of water vapor prior to their later CI (green contour in Figs. 12c and 15a), which subsequently promotes more rapid and vigorous convective development once CI begins. In the highest LLJ case (H21), weak vertical velocity caused by the largest vertical separation between the cold pool and the LLJ core, together with only a modest increase in accumulated moisture, leads to an intermediate fraction of high reflectivity (Figs. 13a and 15a).

To further assess the moisture accumulation process, the low-level moisture (q_v) budget is diagnosed as (Du et al. 2020a,b)

$$\frac{\partial q_v}{\partial t} = -\mathbf{V}\cdot\nabla_h q_v - w\frac{\partial q_v}{\partial z} + A,$$

where $\partial q_v/\partial t$ represents the local tendency of q_v and $-\mathbf{V}\cdot\nabla_h q_v$ and $-w(\partial q_v/\partial z)$ correspond to horizontal and vertical transport, respectively. The additional term $A = \partial q_v/\partial t + \mathbf{V}\cdot\nabla_h q_v + w(\partial q_v/\partial z)$ accounts for subgrid mixing in the boundary layer, condensation or evaporation effects, and computational errors (e.g., interpolation uncertainties).

Figures 15b and 15c present the accumulated q_v tendency during the 10 min prior to CI, averaged over x = 130–180 km at 1–3-km height (dashed red box in Fig. 12a). The total tendency in this region is greater in the higher LLJ cases (H15 and H18), primarily contributed by enhanced horizontal transport associated with the LLJ (Fig. 15b). Although the background environment is horizontally homogeneous, the cold pool circulation or preconvective perturbations can dynamically generate local moisture gradients within the CI region. In contrast, vertical transport dominates moistening in the lower-altitude LLJ cases (H03, H06, and H09), consistent with their stronger vertical velocities near the leading edge of the cold pools (Figs. 13a and 15b).

However, during the mature phase (1–4 h), the H03 simulation exhibits the highest fraction of strong radar reflectivity (>45 or 50 dBZ, Fig. 14b), greatest accumulated rainfall (Fig. 14c), and strongest surface winds exceeding 35 m s^{-1} (Fig. 14d). The time series of average cold pool intensity further indicates that H03 maintains the strongest cold pool intensity throughout the mature period (Fig. 16a).

According to the RKW theory, the development and depth of convection are regulated by the interplay between cold pool intensity (C) and low-level vertical wind shear (ΔU), with the optimal state occurring when the ratio $C/\Delta U$ is approximately 1. To assess the impact of LLJ height on convective development, we calculate this ratio by defining ΔU as the vertical wind difference between the jet core heights (z_m = 300–2100 m for different cases) and the initial cold pool depth (2.5 km). The method aims to test whether the classical RKW theory can be extended or adapted to assess elevated convection influenced by the LLJ. Correspondingly, the revised cold pool intensity (C) is computed by vertically integrating B from z_m to z_c:

$$C = \sqrt{-2\int_{z_m}^{z_c} B\,dz}.$$

The integral is computed over a 20-km horizontal segment rearward of the cold pool leading edge and line-averaged along the y axis. A sensitivity test using a 50-km segment confirmed the consistency of key results and the robustness of the conclusions.

Although the exact definition of the shear layer depth can vary, previous studies have confirmed the practical applicability of the RKW framework (Bryan and Rotunno 2014;

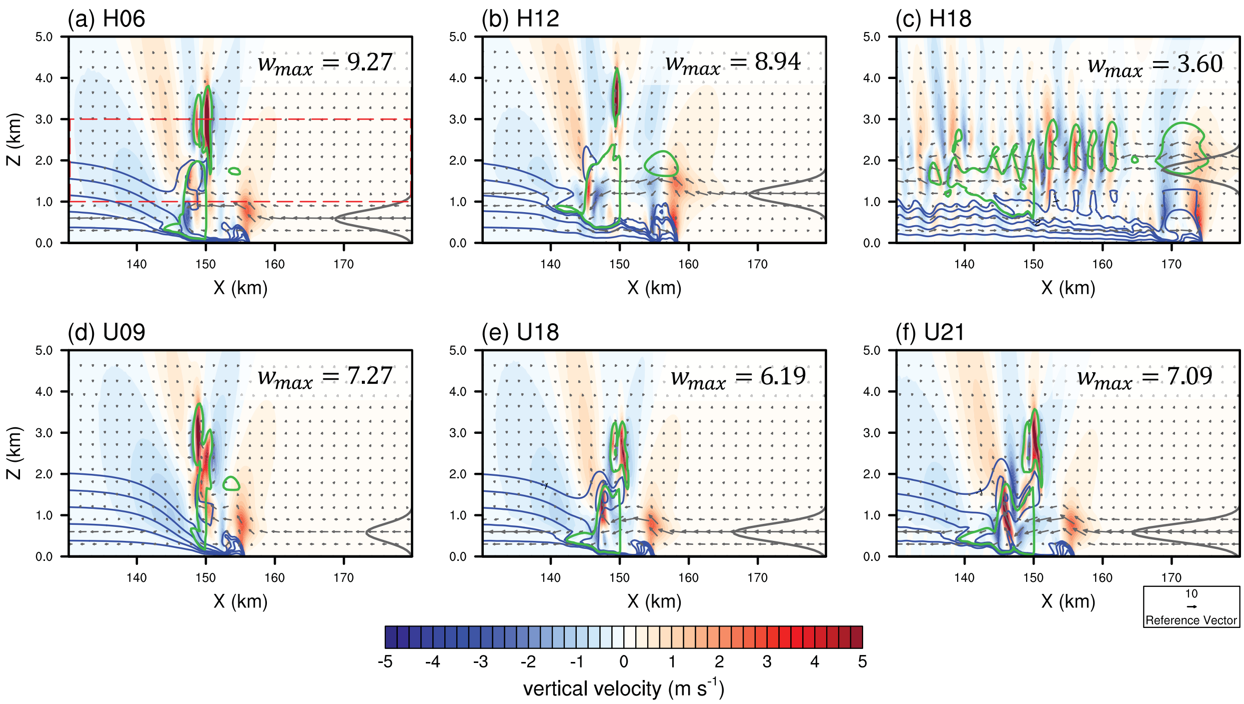

FIG. 12. Line-averaged vertical cross sections of vertical velocity (m s^{-1}; shaded), wind vectors (m s^{-1}), potential temperature perturbation (K; blue contours every -1 K starting from -1 K), and perturbation of water vapor mixing ratio (green contour of 1 g kg^{-1}) for (a) H06, (b) H12, (c) H18, (d) U09, (e) U18, and (f) U21 simulations at 2 min before convection initiation. The gray lines indicate the vertical profiles of horizontal wind speed. The maximum vertical velocity (m s^{-1}) near the cold pool head is given in each panel. The dashed red box in (a) indicates the region for budget analysis in Fig. 15.

Weisman and Rotunno 2004; Bryan et al. 2006). As shown in Fig. 16b, the H03 simulation maintains a $C/\Delta U$ ratio close to 1, particularly during the latter half of the simulation, indicating an optimal environment for convective growth. This near-optimal balance supports vigorous vertical motion along the leading edge of the system, resulting in more intense convective precipitation in that region (Fig. 17a). In contrast, simulations with higher LLJ cores exhibit a declining $C/\Delta U$ ratio, approaching zero due to diminished buoyancy above the elevated jet core. This resulting flow leads to a more strongly tilted ascent and produces weaker convective precipitation (Figs. 17b,c). These findings suggest that achieving the optimal balance between cold pool intensity and vertical shear, and hence supporting more intense convective systems during the mature phase, requires a lower LLJ height (i.e., a stronger cold pool above the LLJ core), as exemplified by the H03 case.

b. *Sensitivity to low-level jet strength*

We further examine the sensitivity of LLJ–cold pool interactions to variations in the strength (u_m) of the LLJ, ranging from -5 to -24 m s^{-1} (Fig. 2c), while keeping the jet core height (z_m = 600 m) and the jet shape (σ = 300 m) constant. Notably, as the LLJ strength increases, horizontal vorticity both above and below the jet core also increases. Across the series of simulations with varying LLJ strengths (Figs. 12d–f), the horizontal position of the cold pool's leading edge and the height of the maximum vertical velocity remain similar (i.e., the cold pools' leading edge is near x = 155 km) due to the nearly zero surface wind speed and constant jet core height. In stronger LLJ cases, the cold pool aloft head appears more elevated, likely due to enhanced jet-core wind speeds and the upward accumulation of cold air within the cold pool.

As shown in Fig. 13b, just before convection occurs, the average vertical motion near the aloft cold pool head is slightly greater in cases with weaker LLJs (U05, U09, and U12), reaching up to 0.5 m s^{-1} at 10 min in the U05 case. Notably, the separation between the surface head and aloft head becomes apparent around 4 min (Fig. 13b), marking a transition in average vertical velocity from surface-head-driven ascent to aloft-head-dominated lifting. The following analysis focuses on the latter. This pronounced uplift in weaker LLJ cases may result from weaker horizontal vorticity below the jet core and reduced horizontal tilting, facilitating deeper vertical parcel lifting and thus earlier convection initiation in these cases (Figs. 13d,f). In contrast, simulations with stronger LLJs (e.g., U18, U21, and U24) exhibit weaker vertical velocities, reduced vertical displacements, and correspondingly delayed convection initiation.

In cases with weaker LLJs, characterized by lower wind speeds and reduced shear, the cold pool experiences minimal weakening and maintains relatively strong intensity throughout the simulation (U05 and U09, Fig. 16c). Regarding the

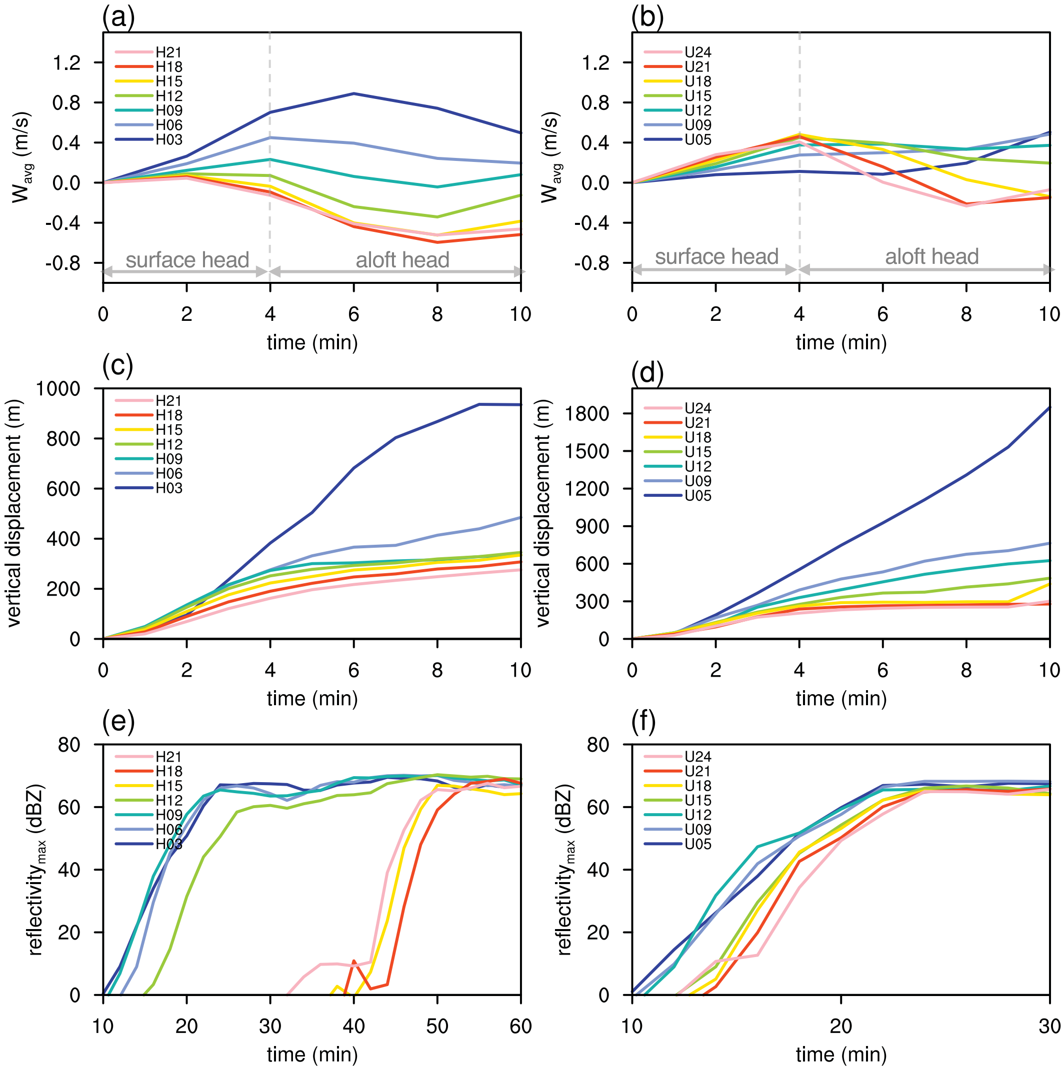

FIG. 13. Time series of (a),(b) average vertical velocity (m s^{-1}) near the initial leading edge of cold pools (x = 148–152 km), (c),(d) maximum vertical displacement (m) for parcels near the jet core, and (e),(f) maximum radar reflectivity (dBZ) for (a),(c),(e) LLJs at varying heights and (b),(d),(f) LLJs at varying strengths.

initial development of the convective system influenced by varying LLJ strengths, stronger LLJ simulations (U15, U18, U21, and U24) exhibit a higher fraction of strong radar reflectivity during the first 30 min after convection initiation (Fig. 18a), indicating rapid system development at this early stage. This behavior is likely due to the slightly greater moisture accumulation before CI (Fig. 15c). The larger accumulated q_v tendency in stronger LLJ simulations (U15, U18, U21, and U24) is primarily attributable to enhanced vertical transport (Fig. 15d).

However, during the mature phase (1–4 h), the overall system strength in stronger LLJ cases does not reach the maximum potential, as reflected in the relatively low values of system-intensity indicators (Figs. 18b–d). Instead, the simulation with a moderate-strength LLJ (e.g., U09) shows higher reflectivity fractions. Similar patterns are observed in accumulated rainfall and maximum surface wind speed (Figs. 18c,d). This enhancement in the U09 case likely results from a near-optimal configuration for upright convective development above the jet core with $C/\Delta U$ approaching 1, especially after 120 min (Fig. 16d), leading to a more intense convective precipitation region (Fig. 17e).

In the weaker LLJ case (U05), $C/\Delta U > 1$ due to smaller vertical shear and stronger cold pool intensity, which inhibits upright ascent (Figs. 16d and 17d). In contrast, stronger LLJ cases (e.g., U18, U21, and U24) display $C/\Delta U < 1$ because of larger vertical wind shear and weaker cold pools (Figs. 16c,d). Here, the enhanced positive vorticity above the jet core interacts with cold pool, producing a weaker convective cell, whereas the larger negative vorticity below the jet core produces a more tilted updraft and a broader stratiform region with slightly higher radar reflectivity (Fig. 17f).

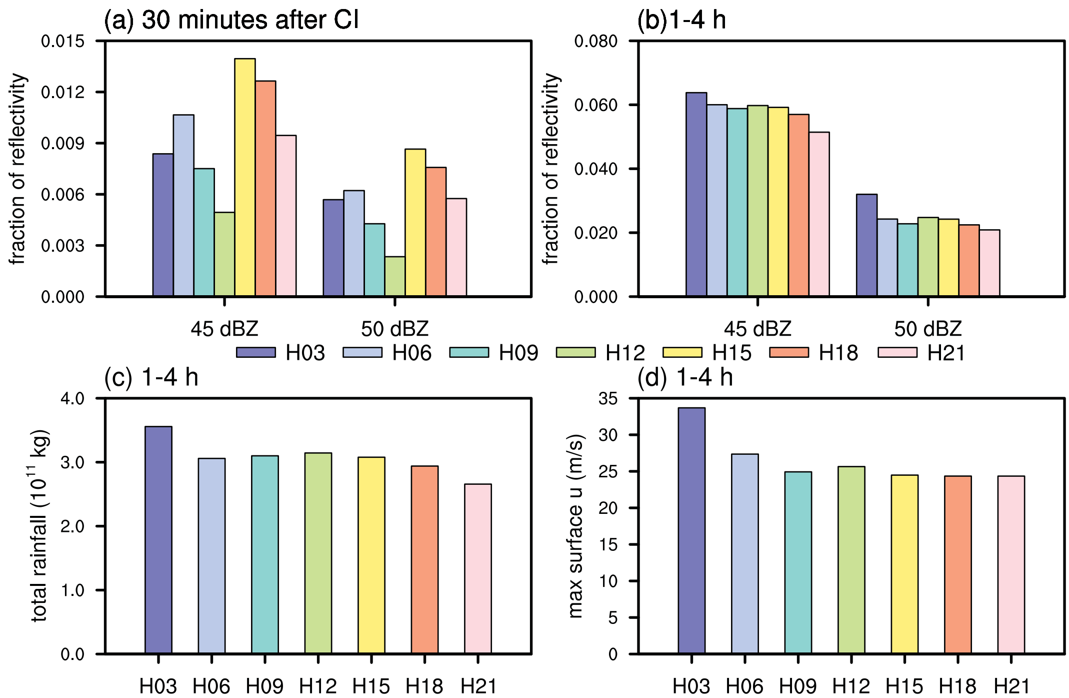

FIG. 14. (a) Fraction of radar reflectivity exceeding 45 and 50 dBZ during the first 30 min after convection initiation, (b) fraction of radar reflectivity exceeding 45 and 50 dBZ, (c) total accumulated rainfall (10^{11} kg), and (d) maximum outflow (m s^{-1}; defined as surface wind relative to the LLJ background flow) at the lowest model level during the mature phase (1–4 h after simulation start) for LLJs with varying heights.

6. Summary and discussion

This study employed Cloud Model 1 to investigate the interaction between low-level jets (LLJs) and cold pools, extending previous research that primarily focused on the effects of unidirectional wind shear on cold pools and squall-line dynamics (Rotunno et al. 1988; Bryan et al. 2006). The analysis highlights how cold pools respond to variations in the height and strength of LLJs, which feature opposing vertical wind shear above and below the jet core, and explores their resulting impacts on the initiation and development of convection.

Using identical initial cold blocks and consistent initial thermodynamic conditions, we conducted a series of idealized three-dimensional numerical simulations to explore how variations in vertical wind profiles affect cold pool structure and associated lifting motions. In simulations without wind and with unidirectional shear, cold pools evolve with either a surface head or an aloft head, each resulting in a single region of vertical motion. Among these cases, the unidirectional shear simulation produces the strongest lifting and earliest convection (Fig. 19a). Even in the mature phase, it continues to yield a more intense convective precipitation area, with larger accumulated rainfall and stronger surface winds (Fig. 19b).

A schematic diagram in Fig. 19c illustrates how an LLJ interacts with a cold pool to drive convection during the initial stage. In contrast to the single head evolution seen in the no-wind and unidirectional shear scenarios, the cold pool influenced by the LLJ typically evolves into a two-step structure, characterized by one surface head and another aloft head. These two heads are accompanied by two separate vertical motion regions. Above the jet core, strong Kelvin–Helmholtz instability occurs near the aloft head's vertical motion region, generating small-scale upward and downward motions that weaken the cold pool. Convection initiation occurs near the aloft head, located at the initial position of the cold pool leading edge. The opposing horizontal vorticities below and above the LLJ core, which interact differently with the negative horizontal vorticity of the cold pool, result in two distinct clusters of parcel trajectories during the initiation phase. Trajectories from above the jet support stronger lifting compared to those from below. At this stage, the elevated convection induced by the LLJ is stronger than the surface-based convection by unidirectional shear, partly because of the broader area of intense convection supported by smaller elevated CIN and larger elevated CAPE.

During the mature phase (1–4 h, Fig. 19d), negative horizontal vorticity associated with the cold pool and the shear below the LLJ core induces multiple tilted parcel trajectories, contributing to an expansion of the stratiform region. Consequently, the LLJ simulation produces a greater fraction of high reflectivity.

To further explore the effects of LLJ characteristics on cold pool dynamics and subsequent convection, a series of sensitivity experiments were conducted by varying LLJ height and strength. In sensitivity experiments with LLJ heights ranging from 300 to 2100 m, both the cold pool head and the height of

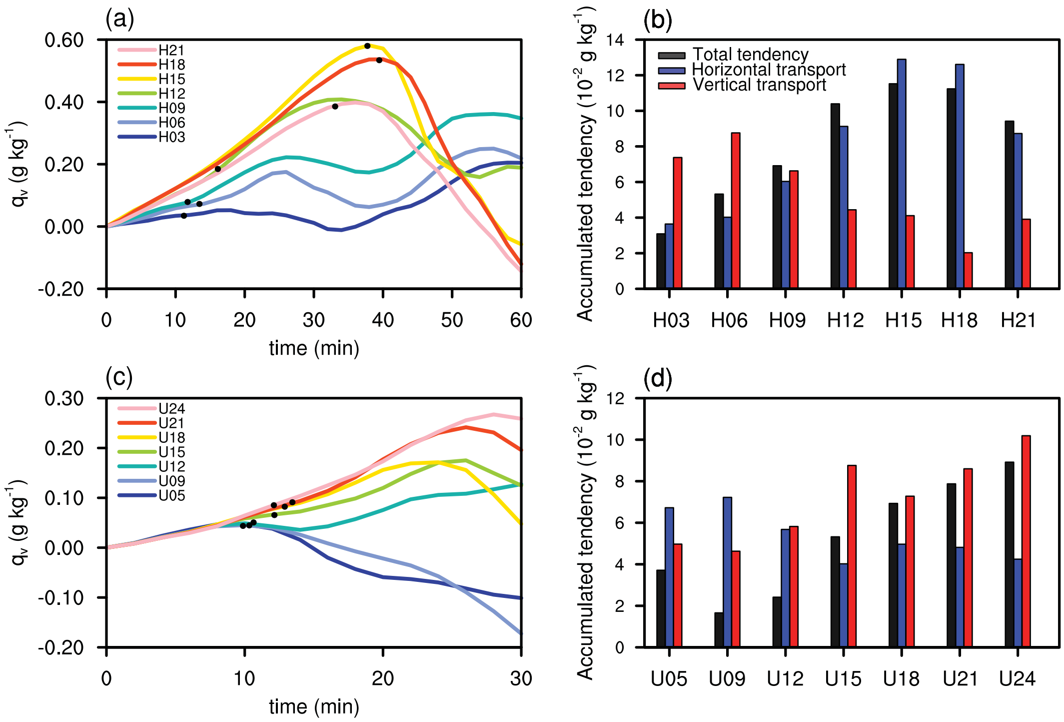

FIG. 15. (a),(c) Domain-averaged perturbation of water vapor mixing ratio (g kg^{-1}) at 1–3-km height over x = 130–180 km. Black dots represent the timing of convection initiation. (b),(d) Accumulated tendency of q_v (black bars; 10^{-2} g kg^{-1}) and its components, including horizontal transport (blue bars) and vertical transport (red bars). (a),(b) LLJ cases with varying core heights; (c),(d) LLJ cases with varying strengths.

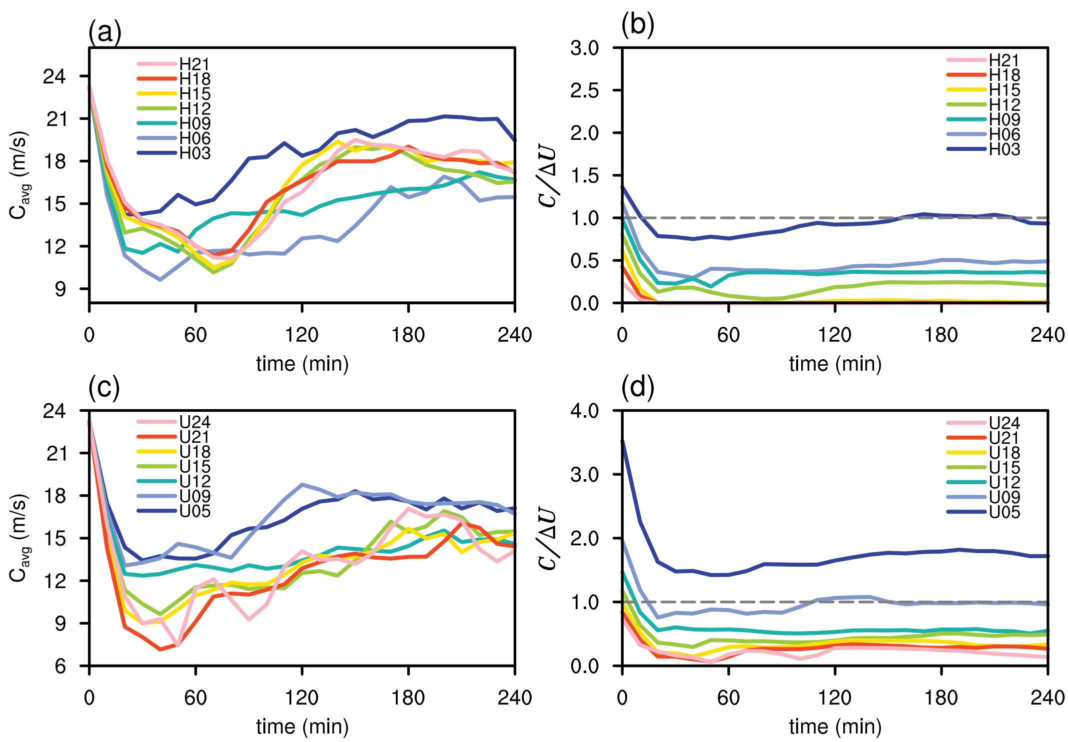

FIG. 16. Time series of (a),(c) average cold pool intensity (m s^{-1}) between the leading edge of the cold pool and 20 km behind it and (b),(d) the ratio of cold pool intensity to the vertical wind shear strength ($C/\Delta U$) for (a),(b) LLJs with varying core heights and (c),(d) LLJs with varying strengths.

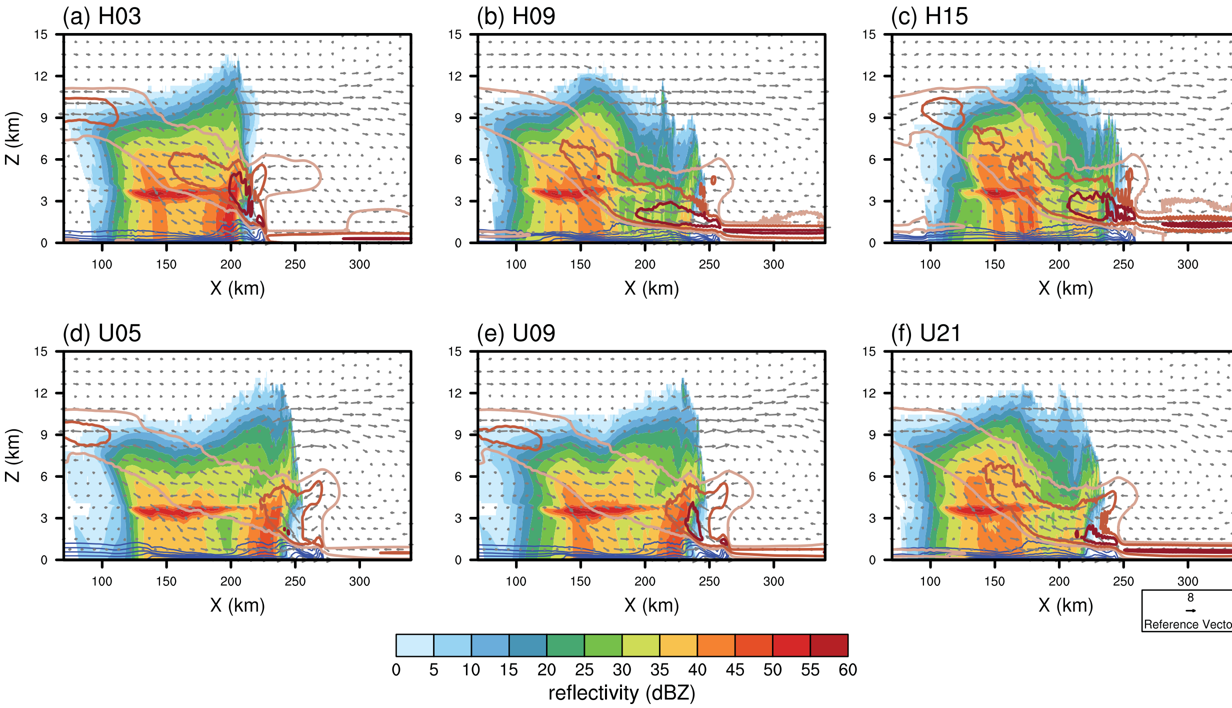

FIG. 17. Line-averaged vertical cross sections at 180 min of radar reflectivity (dBZ; shaded), wind vectors (m s^{-1}), and potential temperature perturbation (K; blue contours every −1 K starting from −2 K) for (a) H03, (b) H09, (c) H15, (d) U05, (e) U09, and (f) U21. Warm-colored contours denote the front-to-rear flow, with wind speed calculated from negative u and positive w components (m s^{-1}; every 4 m s^{-1} starting from 4 m s^{-1}).

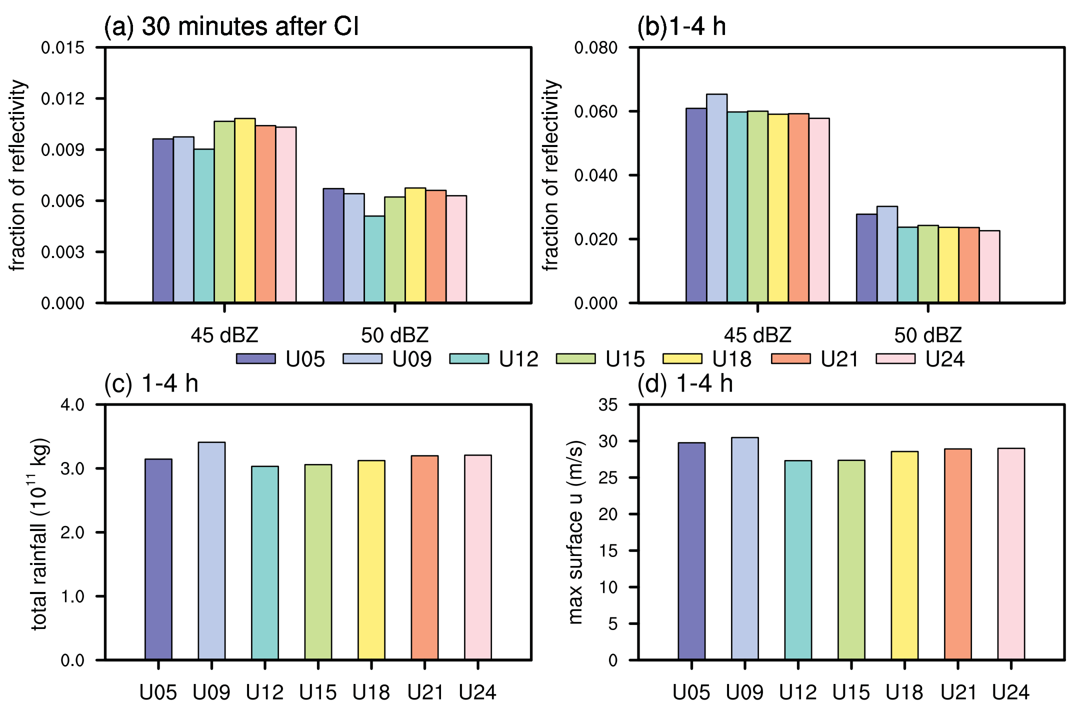

FIG. 18. As in Fig. 14, but for LLJs with varying strengths.

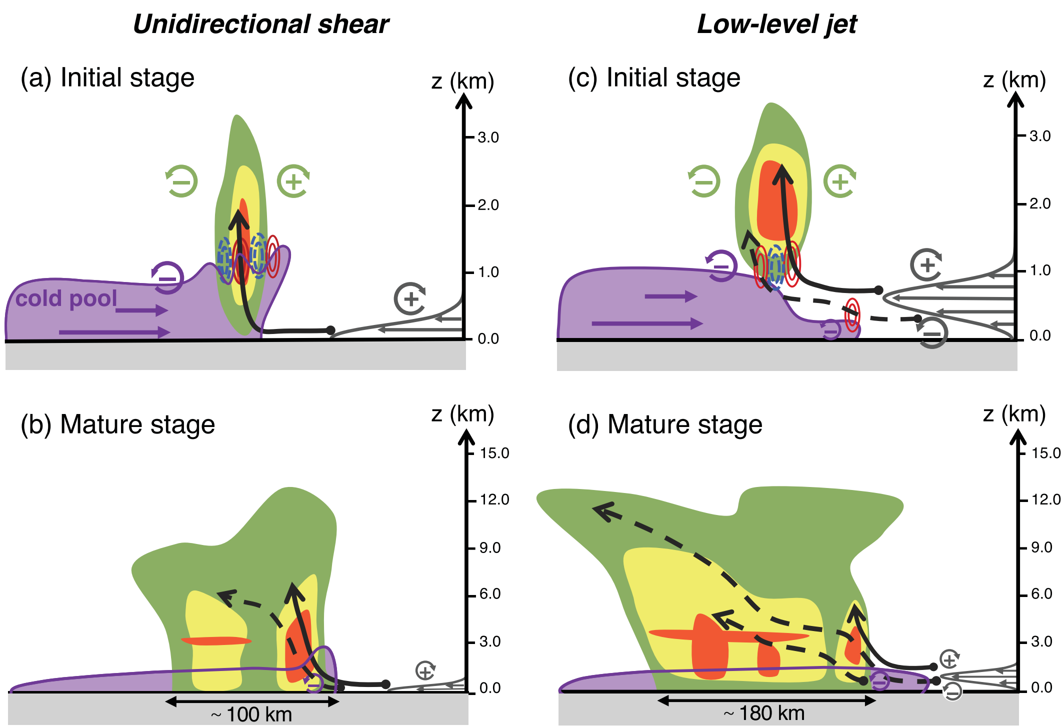

FIG. 19. Schematic diagram showing the interaction between the cold pool and (a),(b) unidirectional shear or (c),(d) LLJ during the (a),(c) initial stage and (b),(d) mature stage. Purple shading indicates the cold pool structure modulated by the effect of unidirectional shear or LLJ, while green–yellow–orange shading indicates radar reflectivity. Purple arrows indicate the horizontal vorticity associated with the cold pool, and gray arrows represent the horizontal vorticity associated with the unidirectional shear or LLJ. The resulting parcel trajectories due to the interaction of unidirectional shear or LLJ and cold pool are shown by black arrows. The red and blue ellipses indicate the updrafts and downdrafts, respectively.

the horizontal wind maximum increase with the LLJ height. Simulations with lower LLJ altitude produce stronger average vertical motion earlier, primarily due to stronger convergence with the cold pool, which leads to earlier convection initiation. Similarly, during the mature phase, the most intense convection occurs in the lowest jet height case (H03), where $C/\Delta U$ approaches the optimal state.

When varying the LLJ strength from -5 to -24 m s^{-1} while keeping the jet height constant, a weaker LLJ produces stronger vertical motion in the early stage, as the reduced horizontal wind shear encourages a more upright tilt and allows more efficient upward motion, favoring earlier convection initiation. Convection intensity peaks in the appropriate LLJ strength experiment (U09) during the mature phase, where the ratio $C/\Delta U \approx 1$ above the jet core, aligning with the optimal state described by the RKW theory, resulting in stronger updraft at the leading edge of the system and enhanced convective precipitation.

This study aims to enhance understanding of LLJ–cold pool interaction in convection initiation and development. However, several limitations remain. First, the simulations do not fully explore the role of cold pool thickness and strength. Preliminary sensitivity experiments on cold pool thickness revealed the significance of the relative heights of cold pools and LLJs, suggesting a need for further investigation. Another limitation involves the use of a single thermodynamic profile. Different LLJ structures may interact differently with varying temperature and moisture soundings. Future studies should explore the sensitivity of LLJ–cold pool interactions across a broader range of thermodynamic environments. In addition, the background wind profiles used in this study are two-dimensional and therefore do not represent the veering with height and time that typically characterizes LLJs in the real atmosphere, arising from the geostrophic balance and boundary layer processes. Such veering modifies both the wind direction and vertical shear, making it important for future research to investigate the influence of more realistic three-dimensional wind profiles and their evolution.

Acknowledgments. This study was supported by the National Key Research and Development Program of China (Grant 2024YFC3013003), the National Natural Science Foundation of China (42475002 and 424B2033), the Guangdong Major Project of Basic and Applied Basic Research (2020B0301030004, 2024A1515510005, and 2025A1515011974), the Project supported by the Southern Marine Science and Engineering Guangdong Laboratory (Zhuhai) (SML2024SP035, SML2024SP012, and 311024001), and the Key Innovation Team of the China Meteorological Administration (CMA2023ZD08). We also acknowledge the high-performance computing support from the School of Atmospheric Sciences of Sun Yat-sen University.

Data availability statement. All simulation data and related codes are archived and available from the corresponding author upon request.

REFERENCES

Alfaro, D. A., and F. Lezana, 2022: A momentum-balance theory for the updraft structure in density currents analogous to squall lines. *Atmósfera*, **35**, 197–220, https://doi.org/10.20937/ATM.52899.

Banta, R. M., Y. L. Pichugina, and R. K. Newsom, 2003: Relationship between low-level jet properties and turbulence kinetic energy in the nocturnal stable boundary layer. *J. Atmos. Sci.*, **60**, 2549–2555, https://doi.org/10.1175/1520-0469(2003)060<2549:RBLJPA>2.0.CO;2.

Borque, P., S. W. Nesbitt, R. J. Trapp, S. Lasher-Trapp, and M. Oue, 2020: Observational study of the thermodynamics and morphological characteristics of a midlatitude continental cold pool event. *Mon. Wea. Rev.*, **148**, 719–737, https://doi.org/10.1175/MWR-D-19-0068.1.

Bryan, G. H., and J. M. Fritsch, 2002: A benchmark simulation for moist nonhydrostatic numerical models. *Mon. Wea. Rev.*, **130**, 2917–2928, https://doi.org/10.1175/1520-0493(2002)130<2917:ABSFMN>2.0.CO;2.

——, and R. Rotunno, 2014: The optimal state for gravity currents in shear. *J. Atmos. Sci.*, **71**, 448–468, https://doi.org/10.1175/JAS-D-13-0156.1.

——, J. C. Knievel, and M. D. Parker, 2006: A multimodel assessment of RKW theory's relevance to squall-line characteristics. *Mon. Wea. Rev.*, **134**, 2772–2792, https://doi.org/10.1175/MWR3226.1.

Chandra, A. S., P. Zuidema, S. Krueger, A. Kochanski, S. P. De Szoeke, and J. Zhang, 2018: Moisture distributions in tropical cold pools from equatorial Indian Ocean observations and cloud-resolving simulations. *J. Geophys. Res. Atmos.*, **123**, 11 445–11 465, https://doi.org/10.1029/2018JD028634.

Charba, J., 1974: Application of gravity current model to analysis of squall-line gust front. *Mon. Wea. Rev.*, **102**, 140–156, https://doi.org/10.1175/1520-0493(1974)102<0140:AOGCMT>2.0.CO;2.

Chen, C., 1995: Numerical simulations of gravity currents in uniform shear flows. *Mon. Wea. Rev.*, **123**, 3240–3253, https://doi.org/10.1175/1520-0493(1995)123<3240:NSOGCI>2.0.CO;2.

Chen, G., H. Iwai, S. Ishii, K. Saito, H. Seko, W. Sha, and T. Iwasaki, 2019: Structures of the sea-breeze front in dual-Doppler lidar observation and coupled mesoscale-to-LES modeling. *J. Geophys. Res. Atmos.*, **124**, 2397–2413, https://doi.org/10.1029/2018JD029017.

Coniglio, M. C., D. J. Stensrud, and M. B. Richman, 2004: An observational study of derecho-producing convective systems. *Wea. Forecasting*, **19**, 320–337, https://doi.org/10.1175/1520-0434(2004)019<0320:AOSODC>2.0.CO;2.

Droegemeier, K. K., and R. B. Wilhelmson, 1987: Numerical simulation of thunderstorm outflow dynamics. Part I: Outflow sensitivity experiments and turbulence dynamics. *J. Atmos. Sci.*, **44**, 1180–1210, https://doi.org/10.1175/1520-0469(1987)044<1180:NSOTOD>2.0.CO;2.

Du, Y., and R. Rotunno, 2014: A simple analytical model of the nocturnal low-level jet over the Great Plains of the United States. *J. Atmos. Sci.*, **71**, 3674–3683, https://doi.org/10.1175/JAS-D-14-0060.1.

——, G. Chen, B. Han, C. Mai, L. Bai, and M. Li, 2020a: Convection initiation and growth at the coast of South China. Part I: Effect of the marine boundary layer jet. *Mon. Wea. Rev.*, **148**, 3847–3869, https://doi.org/10.1175/MWR-D-20-0089.1.

——, ——, ——, L. Bai, and M. Li, 2020b: Convection initiation and growth at the coast of South China. Part II: Effects of the terrain, coastline, and cold pools. *Mon. Wea. Rev.*, **148**, 3871–3892, https://doi.org/10.1175/MWR-D-20-0090.1.

Evans, J. S., and C. A. Doswell, 2001: Examination of derecho environments using proximity soundings. *Wea. Forecasting*, **16**, 329–342, https://doi.org/10.1175/1520-0434(2001)016<0329:EODEUP>2.0.CO;2.

Feng, Z., S. Hagos, A. K. Rowe, C. D. Burleyson, M. N. Martini, and S. P. Szoeke, 2015: Mechanisms of convective cloud organization by cold pools over tropical warm ocean during the AMIE/DYNAMO field campaign. *J. Adv. Model. Earth Syst.*, **7**, 357–381, https://doi.org/10.1002/2014MS000384.

French, A. J., and M. D. Parker, 2010: The response of simulated nocturnal convective systems to a developing low-level jet. *J. Atmos. Sci.*, **67**, 3384–3408, https://doi.org/10.1175/2010JAS3329.1.

Fritsch, J. M., and G. S. Forbes, 2001: Mesoscale convective systems. Severe Convective Storms, Meteor. Monogr., No. 50, Amer. Meteor. Soc., 323–358, https://doi.org/10.1175/0065-9401-28.50.323.

Fu, D., Y. Du, C. Mai, M. Li, and C. Li, 2025: Impact of boundary layer jets on cold pool characteristics observed from the 356-m high Shenzhen Meteorological Tower. *J. Geophys. Res. Atmos.*, **130**, e2024JD042926, https://doi.org/10.1029/2024JD042926.

Goff, R. C., 1976: Vertical structure of thunderstorm outflows. *Mon. Wea. Rev.*, **104**, 1429–1440, https://doi.org/10.1175/1520-0493(1976)104<1429:VSOTO>2.0.CO;2.

Grant, L. D., and S. C. van den Heever, 2016: Cold pool dissipation. *J. Geophys. Res. Atmos.*, **121**, 1138–1155, https://doi.org/10.1002/2015JD023813.

Hitchcock, S. M., and R. S. Schumacher, 2020: Analysis of back-building convection in simulations with a strong low-level stable layer. *Mon. Wea. Rev.*, **148**, 3773–3797, https://doi.org/10.1175/MWR-D-19-0246.1.

Hu, X.-M., P. M. Klein, M. Xue, J. K. Lundquist, F. Zhang, and Y. Qi, 2013: Impact of low-level jets on the nocturnal urban heat island intensity in Oklahoma City. *J. Appl. Meteor. Climatol.*, **52**, 1779–1802, https://doi.org/10.1175/JAMC-D-12-0256.1.

Klemp, J. B., and R. B. Wilhelmson, 1978: The simulation of three-dimensional convective storm dynamics. *J. Atmos. Sci.*, **35**, 1070–1096, https://doi.org/10.1175/1520-0469(1978)035<1070:TSOTDC>2.0.CO;2.

Li, H., Y. Huang, S. Hu, N. Wu, X. Liu, and H. Xiao, 2021: Roles of terrain, surface roughness, and cold pool outflows in an extreme rainfall event over the coastal region of South China. *J. Geophys. Res. Atmos.*, **126**, e2021JD035556, https://doi.org/10.1029/2021JD035556.

Luiz, E. W., and S. Fiedler, 2024: Global climatology of low-level-jets: Occurrence, characteristics, and meteorological drivers. *J. Geophys. Res. Atmos.*, **129**, e2023JD040262, https://doi.org/10.1029/2023JD040262.

Luo, Y., and Y. Du, 2023: The roles of low-level jets in "21·7" Henan extremely persistent heavy rainfall event. *Adv. Atmos. Sci.*, **40**, 350–373, https://doi.org/10.1007/s00376-022-2026-1.

Mai, C., Y. Du, M. Li, G. Chen, L. Su, C. Li, D. Fu, and H. Kong, 2025: Cold pools detected by a 356-m meteorological tower in a monsoon coastal region. *Adv. Atmos. Sci.*, **42**, 2235–2246, https://doi.org/10.1007/s00376-025-4446-1.

Marion, G. R., and R. J. Trapp, 2019: The dynamical coupling of convective updrafts, downdrafts, and cold pools in simulated supercell thunderstorms. *J. Geophys. Res. Atmos.*, **124**, 664–683, https://doi.org/10.1029/2018JD029055.

Parker, D. J., 1996: Cold pools in shear. *Quart. J. Roy. Meteor. Soc.*, **122**, 1655–1674, https://doi.org/10.1002/qj.49712253509.

Parker, M. D., 2008: Response of simulated squall lines to low-level cooling. *J. Atmos. Sci.*, **65**, 1323–1341, https://doi.org/10.1175/2007JAS2507.1.

Plant, R. S., and G. J. Keith, 2007: Occurrence of Kelvin-Helmholtz billows in sea-breeze circulations. *Bound.-Layer Meteor.*, **122**, 1–15, https://doi.org/10.1007/s10546-006-9089-x.

Purdom, J. F. W., 1976: Some uses of high-resolution GOES imagery in the mesoscale forecasting of convection and its behavior. *Mon. Wea. Rev.*, **104**, 1474–1483, https://doi.org/10.1175/1520-0493(1976)104<1474:SUOHRG>2.0.CO;2.

Rotunno, R., J. B. Klemp, and M. L. Weisman, 1988: A theory for strong, long-lived squall lines. *J. Atmos. Sci.*, **45**, 463–485, https://doi.org/10.1175/1520-0469(1988)045<0463:ATFSLL>2.0.CO;2.

Schumacher, R. S., 2009: Mechanisms for quasi-stationary behavior in simulated heavy-rain-producing convective systems. *J. Atmos. Sci.*, **66**, 1543–1568, https://doi.org/10.1175/2008JAS2856.1.

Sha, W., T. Kawamura, and H. Ueda, 1991: A numerical study on sea/land breezes as a gravity current: Kelvin–Helmholtz billows and inland penetration of the sea-breeze front. *J. Atmos. Sci.*, **48**, 1649–1665, https://doi.org/10.1175/1520-0469(1991)048<1649:ANSOSB>2.0.CO;2.

Shapiro, A., and E. Fedorovich, 2010: Analytical description of a nocturnal low-level jet. *Quart. J. Roy. Meteor. Soc.*, **136**, 1255–1262, https://doi.org/10.1002/qj.628.

Simoes-Sousa, I. T., A. Tandon, J. Buckley, D. Sengupta, J. Sree Lekha, E. Shroyer, and S. P. de Szoeke, 2022: Atmospheric cold pools in the Bay of Bengal. *J. Atmos. Sci.*, **80**, 167–180, https://doi.org/10.1175/JAS-D-22-0041.1.

Stensrud, D. J., M. C. Coniglio, R. P. Davies-Jones, and J. S. Evans, 2005: Comments on "'A theory for strong long-lived squall lines' revisited". *J. Atmos. Sci.*, **62**, 2989–2996, https://doi.org/10.1175/JAS3514.1.

Thorpe, A. J., M. J. Miller, and M. W. Moncrieff, 1982: Two-dimensional convection in non-constant shear: A model of mid-latitude squall lines. *Quart. J. Roy. Meteor. Soc.*, **108**, 739–762, https://doi.org/10.1002/qj.49710845802.

Torri, G., Z. Kuang, and Y. Tian, 2015: Mechanisms for convection triggering by cold pools. *Geophys. Res. Lett.*, **42**, 1943–1950, https://doi.org/10.1002/2015GL063227.

Trapp, R. J., and J. M. Woznicki, 2017: Convectively induced stabilizations and subsequent recovery with supercell thunderstorms during the Mesoscale Predictability Experiment (MPEX). *Mon. Wea. Rev.*, **145**, 1739–1754, https://doi.org/10.1175/MWR-D-16-0266.1.

Trier, S. B., C. A. Davis, D. A. Ahijevych, M. L. Weisman, and G. H. Bryan, 2006: Mechanisms supporting long-lived episodes of propagating nocturnal convection within a 7-day WRF model simulation. *J. Atmos. Sci.*, **63**, 2437–2461, https://doi.org/10.1175/JAS3768.1.

Vera, C., and Coauthors, 2006: The South American low-level jet experiment. *Bull. Amer. Meteor. Soc.*, **87**, 63–78, https://doi.org/10.1175/BAMS-87-1-63.

Weisman, M. L., 1992: The role of convectively generated rear-inflow jets in the evolution of long-lived mesoconvective systems. *J. Atmos. Sci.*, **49**, 1826–1847, https://doi.org/10.1175/1520-0469(1992)049<1826:TROCGR>2.0.CO;2.

——, 1993: The genesis of severe, long-lived bow echoes. *J. Atmos. Sci.*, **50**, 645–670, https://doi.org/10.1175/1520-0469(1993)050<0645:TGOSLL>2.0.CO;2.

——, and J. B. Klemp, 1982: The dependence of numerically simulated convective storms on vertical wind shear and buoyancy. *Mon. Wea. Rev.*, **110**, 504–520, https://doi.org/10.1175/1520-0493(1982)110<0504:TDONSC>2.0.CO;2.

——, and R. Rotunno, 2004: "A theory for strong long-lived squall lines" revisited. *J. Atmos. Sci.*, **61**, 361–382, https://doi.org/10.1175/1520-0469(2004)061<0361:ATFSLS>2.0.CO;2.

——, J. B. Klemp, and R. Rotunno, 1988: Structure and evolution of numerically simulated squall lines. *J. Atmos. Sci.*, **45**, 1990–2013, https://doi.org/10.1175/1520-0469(1988)045<1990:SAEONS>2.0.CO;2.

——, W. C. Skamarock, and J. B. Klemp, 1997: The resolution dependence of explicitly modeled convective systems. *Mon. Wea. Rev.*, **125**, 527–548, https://doi.org/10.1175/1520-0493(1997)125<0527:TRDOEM>2.0.CO;2.

Whiteman, C. D., X. Bian, and S. Zhong, 1997: Low-level jet climatology from enhanced rawinsonde observations at a site in the southern Great Plains. *J. Appl. Meteor.*, **36**, 1363–1376, https://doi.org/10.1175/1520-0450(1997)036<1363:LLJCFE>2.0.CO;2.

Xu, Q., 1992: Density currents in shear flows-a two-fluid model. *J. Atmos. Sci.*, **49**, 511–524, https://doi.org/10.1175/1520-0469(1992)049<0511:DCISFA>2.0.CO;2.

Xue, M., 2002: Density currents in shear flows: Effects of rigid lid and cold-pool internal circulation, and application to squall line dynamics. *Quart. J. Roy. Meteor. Soc.*, **128**, 47–73, https://doi.org/10.1256/00359000260498789.

Yang, H., and Y. Du, 2026: Distinct convection initiation near and far ahead of an idealized squall line. *J. Atmos. Sci.*, **83**, 151–168, https://doi.org/10.1175/JAS-D-25-0073.1.

Zhao, X., A. Lai, X. Wang, S. Li, X. Wang, D. He, and W. Zhou, 2024: The role of the cold pool in a mountain-to-plain and plain-to-mountain squall line case in the south of the Yangtze River in China. *Atmos. Res.*, **300**, 107236, https://doi.org/10.1016/j.atmosres.2024.107236.

Zipser, E. J., 1977: Mesoscale and convective–scale downdrafts as distinct components of squall-line structure. *Mon. Wea. Rev.*, **105**, 1568–1589, https://doi.org/10.1175/1520-0493(1977)105<1568:MACDAD>2.0.CO;2.